TanSat-2: a new satellite for mapping solar-induced chlorophyll fluorescence at both red and far-red bands with high spatio-temporal resolution

Dianrun Zhao[1,2,3], Shanshan Du[1,2], Chu Zou[1,2,3], Longfei Tian[4], Meng Fan[1,5], Yulu Du[1,2,3], and Liangyun Liu[1,2,3]

[1]Key Laboratory of Digital Earth Science, Aerospace Information Research Institute, Chinese Academy of Sciences, Beijing 100094, China;
[2]International Research Center of Big Data for Sustainable Development Goals, Beijing 100094, China
[3]University of Chinese Academy of Sciences, Beijing 100049, China
[4]Innovation Academy for Microsatellites of CAS, Shanghai 201203, China
[5]State Key Laboratory of Remote Sensing Science, Aerospace Information Research Institute, Chinese Academy of Sciences, Beijing 100101, China

Correspondence to: Shanshan Du (duss@radi.ac.cn)

Abstract. Global observations of solar-induced chlorophyll fluorescence (SIF) serve as a robust proxy for monitoring vegetation photosynthetic activity and elucidating the terrestrial carbon cycle. To date, several atmospheric remote sensing satellites have been deployed to generate global SIF products. However, accurate mapping of dual-band (red and far-red) SIF with daily temporal resolution and kilometer-level spatial resolution remains a critical gap, despite its significance for various applications. The Chinese next-generation greenhouse gas monitoring satellite, TanSat-2, is set to succeed the original TanSat satellite, aiming to record the fraction of greenhouse gases, pollutants, and SIF measurements from space. According to current schedules, TanSat-2 is slated for launch in 2026. This satellite will feature a wide swath of 2900 km, high spatial resolution of 2 km at an orbit altitude of 7000 km, and near-daily global coverage. TanSat-2 is equipped with two spectral channels—747–777 nm and 672–702 nm—operating at a spectral resolution of 0.12 nm, thereby offering significant potential for mapping SIF in both the red and far-red bands. In this study, we explore the prospective capabilities of TanSat-2 for SIF retrieval through simulation experiments. First, we simulated the satellite's radiative transfer processes using the Moderate Resolution Atmospheric Transmission 5 (MODTRAN 5) and Soil Canopy Observation of Photosynthesis and Energy (SCOPE) models. An end-to-end orbit simulation dataset for TanSat-2 was generated by aggregating global bottom-of-atmosphere (BOA) reflectance, meteorological datasets, and the global OCO-2 SIF dataset (GOSIF). We then assessed the theoretical accuracy of TanSat-2 based on this spectral simulation dataset, yielding root mean square error (RMSE) values of 0.24 and 0.19 mW m^{-2} sr^{-1} nm^{-1} for SIF retrievals at 740 nm and 685 nm, respectively. Finally, we examined the global prospects of TanSat-2 SIF retrievals using the end-to-end orbit simulations. Comparisons between the anticipated TanSat-2 SIF retrievals and GOSIF inputs revealed excellent correlation at both bands, with R^2 values of 0.88 and 0.61, and RMSE values of 0.082 and 0.061 mW m^{-2} sr^{-1} nm^{-1}, respectively. Thus, TanSat-2 is poised to provide a valuable data resource for reliable SIF retrievals in the red and far-red bands, characterized by high spatio-temporal resolution on a global scale.

1 Introduction

Solar-induced chlorophyll fluorescence (SIF) is a subtle emission produced by chlorophyll during photosynthesis, spanning approximately 640–850 nm with distinct peaks around 685 and 740 nm (Mohammed et al., 2019; Guanter et al., 2014;). Recent advancements in hyperspectral satellite sensor technology have made global SIF monitoring a focal point of research (Guanter et al., 2012; Köhler et al., 2015b). SIF mapping from satellites offers a robust tool for assessing global vegetation photosynthetic activity and understanding the terrestrial carbon cycle (Zheng et al., 2024).

Table 1 outlines the specifications of satellites and instruments capable of SIF retrieval. The first global SIF map utilized data from the Japanese Greenhouse Gases Observing SATellite (GOSAT), which launched in 2009. GOSAT operates within a spectral range of 754-773 nm and boasts a spectral resolution of 0.025 nm. Its coverage includes a swath width of 790 km and a spatial resolution of 10.5 km diameter, providing moderate-resolution surface data but lacking in continuous global coverage due to periodic sampling intervals (Frankenberg et al., 2011b; Joiner et al., 2011). Conversely, the Orbiting Carbon Observatory-2 (OCO-2) enhances SIF retrieval capabilities with a 100-fold increase in observations compared to GOSAT, although it has a narrower swath of 10.3 km and a pixel size of 1.3 km × 2.25 km, still falling short of continuous global coverage (Frankenberg et al., 2014a; Sun et al., 2017). The subsequent OCO-3, launched in 2019, maintains similar specifications with a swath width around 10 km and a spatial resolution of 1.6 × 2.2 km (Taylor et al., 2020). Launched in 2016, the Chinese Carbon Dioxide Observation Satellite Mission (TanSat) covers a spectral range of 758-778 nm and offers a spectral resolution of 0.044 nm, with a swath width of 20 km and a spatial resolution of 2 km, facilitating SIF retrieval at Fe (centered at 758.8 nm) and KI (centered at 771 nm) Fraunhofer lines (Du et al., 2018). The recently launched First Terrestrial Ecosystem Carbon Inventory Satellite (TECIS-1) in August 2022, operates across 670-780 nm with a swath width of 34 km and an unprecedented spatial resolution of 375 m, suitable for dual-band (red and far-red) SIF retrieval (Du et al., 2020; Zou et al., 2021; Du et al., 2022). The Global Ozone Monitoring Experiment 2 (GOME-2) on the MetOp-A/B satellites, launched by Europe in 2007, operates in the red and near-infrared spectra (Joiner et al., 2013, 2016; Köhler et al., 2015). Initially featuring a pixel resolution of 40 km × 80 km, this was later refined to 40 km × 40 km for MetOp-A starting July 2013. GOME-2 scans the Earth with a 1920 km wide swath, achieving global coverage approximately every 1.5 days. Despite its relatively coarse resolution, GOME-2, along with the Scanning Imaging Absorption Spectrometer for Atmospheric Chartography (SCIAMACHY) aboard ENVISAT, has facilitated the creation of two global, spatially continuous solar-induced fluorescence (SIF) datasets. SCIAMACHY covers a spectral range of 595–812 nm at 0.48 nm resolution, extending across a 2800 km swath with pixel sizes varying from 30 km × 240 km to 30 km × 60 km (Joiner et al., 2012; Köhler et al., 2015a).

Launched in 2017, the TROPOspheric Monitoring Instrument (TROPOMI) on the Sentinel-5 Precursor offers unprecedented detail with its 2600 km swath and high spatial resolution of 3.5 km × 5.5/7.5 km, ensuring daily global coverage (Guanter et al., 2011; Köhler et al., 2018; Zhao et al., 2022a). As the first imaging spectrometer of its kind, TROPOMI provides kilometer-level spatial resolution, continuous spectral sampling from 675 to 775 nm at a resolution of 0.38 nm. While it delivers enhanced radiometric sensitivity and broad spectral coverage, its spectral resolution remains suboptimal for detailed red SIF retrieval (Zou et al., 2022).

Looking ahead to post-2025, the planned FLEX mission aims to survey the 500–780 nm range with an adaptable spectral resolution between 0.3 nm and 2.0 nm. It will feature a swath width of at least 150 km and a spatial resolution as fine as 0.3 km (Vicent et al., 2016; Coppo et al., 2017). This mission is set to significantly advance our monitoring of photosynthesis and vegetation health. Concurrently, the CO2M mission, slated for a 2026 launch, will offer high spectral and spatial resolutions. However, its narrower swath will limit its coverage area, impacting its ability to monitor SIF extensively.

The next-generation Chinese greenhouse gas monitoring satellite, TanSat-2, is scheduled for launch in 2026 as the successor to the original TanSat satellite. Unlike its predecessor, which primarily focused on carbon dioxide monitoring, TanSat-2 is designed

to facilitate global carbon stocktaking. To achieve this objective, it will combine a wide swath of 2,900 km with high spatial resolution (2 km at an orbit altitude of 7000 km) and near-daily global coverage. Compared to the TROPOMI satellite, TanSat-2's broader swath and enhanced spatial resolution are expected to yield more frequent and detailed observations, thereby improving the quality and utility of data collected for environmental monitoring and research. Additionally, TanSat-2 will record upwelling radiances with a spectral resolution of 0.12 nm across both the O_2-A and O_2-B bands. This extensive spectral coverage and high spectral resolution will allow for a more accurate exploitation of the entire SIF spectrum, rather than being limited to the far-red SIF.

Red SIF is recognized for its superior ability to reflect the biochemical characteristics and photosynthetic capacity of vegetation compared to far-red SIF (Verrelst et al., 2015). However, the absorption features in the red region tend to be narrower and less pronounced than those in the far-red band, complicating the retrieval of SIF in the red spectral region. Furthermore, there are currently few satellites equipped with red SIF bands, resulting in ongoing challenges with poor signal quality and insufficient accuracy at the application level for existing red SIF products (Dechant et al., 2022). Consequently, most satellite-based SIF products have focused on the far-red band. Some studies have suggested that a payload with high spectral resolution (0.1 nm) and a high signal-to-noise ratio (SNR > 1500) could fulfill the requirements for retrieving red SIF, as demonstrated through simulations of satellite remote sensing accuracy (Zou et al., 2022). Presently, existing spaceborne imaging spectrometers, including TROPOMI, TECIS-1, GOME-2, and FLEX, do not meet the stringent spectral requirements necessary for effective red SIF retrieval. Therefore, TanSat-2 is poised to be the only satellite capable of delivering high-quality SIF retrievals for both the red and far-red bands (Zou et al., 2022). With its wide swath of 2,900 km and spatial resolution of 2 km, TanSat-2 is anticipated to significantly enhance global SIF observation capabilities compared to all current satellites.

In this study, we aim to (1) generate an end-to-end orbit simulation dataset for the TanSat-2 satellite; (2) optimize the empirical parameters of the data-driven algorithm for red and far-red SIF retrieval; (3) investigate TanSat-2's potential for improving SIF retrieval accuracy; and (4) explore the prospects of TanSat-2 for global-scale SIF monitoring.

Table 1. Specifications of the launched or scheduled satellites with the potential of SIF retrieval.

Satellite/Sensor	Launch time	Spectral coverage (nm)	Spectral resolution (nm)	Swath (km)	Spatial resolution (km)	Overpass time
GOSAT	2009.01	754-773	0.025	790	10.5	13:00
OCO-2	2014	757-775	0.042	10.3	1.3×2.25	13:30
OCO-3	2019.05	757-771	0.042	~10	1.6×2.2	13:30
TanSat	2016.12	758-778	0.044	20	2	13:30
TECIS-1	2022.08	670-780	0.3	34	0.345	10:30
SCIAMACHY	2002.03	595-812	0.48	2800	30×240/60	10:30
GOME-2	2007.01	590-790	0.5	1920	40×80/40	9:30
TROPOMI	2017.11	661-775	0.37	2600	3.5×5.5/7.5	13:30
FLEX	>2025	500-780	0.3-2.0	300	0.3	10:00
CO2M	2026	747-773	0.12	>250	2	-
TanSat-2	2026	672-702 747-777	0.12	2900	2	13:30

2 Materials

2.1 TanSat-2 satellite

The second iteration of China's TanSat satellite, TanSat-2, operates in a critically inclined sun-synchronous orbit with an inclination of approximately 116.6°. Positioned primarily above the Northern Hemisphere, the satellite is strategically placed to monitor densely populated regions, such as Asia, North America, and Europe, where human activities are concentrated. By meticulously adjusting various orbital elements, including inclination, semi-major axis, and eccentricity, TanSat-2 achieves a nodal precession rate of roughly 0.98° per day eastward. This specific configuration preserves the sun-synchronous nature of the orbit, ensuring that observations are made under consistent solar illumination at the same local time each day. The parameters of this orbit are detailed in Table 2, which facilitates the simulation of the satellite's trajectory.

Table 2. TanSat-2 orbit parameters

Orbit parameters	Value
Apogee altitude	7443 km
Perigee altitude	702 km
Inclination	116.565 deg
Argument of perigee	220 deg
Local time of ascending node	About 13:05

Equipped with four advanced payloads, TanSat-2 surpasses its predecessor in capability. These include the Ultra-Wide Swath Hyperspectral imager for co-monitoring GHG and NO_2 (Uwhigo), which monitors greenhouse gases (GHGs) and nitrogen dioxide (NO_2) across a 1500 km swath with a 4 km resolution. The High-resolution Hyperspectral imager for monitor Hotspot emission (H3imager) targets GHG emissions from localized sources with a 50 km swath and 500 m resolution. The Cloud and Aerosol polarization hyperspectral imager (CAPHI) is designed to assess aerosol optical depth (AOD) and cloud coverage, while the dual-band SIF imaging spectrometer (DuSIFIS) focuses on far-red and red SIF detection. The specifications for the DuSIFIS payload are provided in Table 3.

Table 3. Preliminary specifications for the O_2 bands included in the TanSat-2 payloads.

Bands	Spectral coverage (nm)	Spectral resolution (nm)	Spectral sampling interval (nm)	SNR	Spatial resolution	Swath
O_2-A	747-777	0.12	0.04	500 at $6.4*10^{19}$ photon/sec/m^2/sr/um	2 km at 7000 km orbit altitude	2900 km
O_2-B	672-702			780 at $1.6*10^{20}$ photon/sec/m^2/sr/um		

2.2 Simulation Experiments

2.2.1 Satellite radiative transfer simulation of TanSat-2

Assuming a Lambertian surface, the top-of-atmosphere (TOA) radiance observed by an instrument over vegetative targets can be approximated as (Guanter et al., 2010; Liu et al., 2014;):

$$L_{TOA} \approx \frac{I_{sol}*\mu_0}{\pi} * \left[\rho_0 + \frac{\rho_s*T_{\downarrow\uparrow}}{1-S*\rho_s}\right] + \frac{SIF*T_{\uparrow}}{1-S*\rho_s} \quad (1)$$

where I_{sol} is the extraterrestrial solar radiation, and μ_0 denotes the cosine of the solar zenith angle (SZA). Reflectance from the atmospheric path is indicated by ρ_0, and surface reflectance is denoted by ρ_s. The spherical albedo of the atmosphere is symbolized by S. The total atmospheric transmittance, $T_{\downarrow\uparrow}$, encompasses both downward and upward transmission, with $T_{\uparrow}$ specifically referring to the transmission from the surface to the sensor. The fluorescence signal (SIF), emitted at the top of the canopy (TOC), should be excluded when modeling radiance for areas without vegetation.

The Soil Canopy Observation Photochemistry and Energy Flux (SCOPE) model (van der Tol et al., 2009) is capable of simulating vegetation canopy reflectance spectra and SIF under diverse canopy structures and leaf biochemical conditions, including leaf optical properties (e.g., chlorophyll content, dry matter) and canopy structural parameters (e.g., leaf area index, canopy height). ~~The Soil Canopy Observation Photochemistry and Energy Flux (SCOPE) model developed by van der Tol et al. (2009) and is capable of simulating vegetation canopy reflectance spectra and SIF signals under various conditions, including different canopy structures and leaf biochemical properties. The model incorporates atmospheric radiative transfer functions derived from the Moderate resolution atmospheric TRANsmission (MODTRAN5) (Berk et al., 1998, 2000), to perform top-of-atmosphere radiance forward simulations based on specific surface properties. Employing the most recent version of the MODTRAN interrogation technique (MIT) (Verhoef and Bach, 2012; Verhoef et al., 2018), 18 spectral transfer functions were extracted and applied within the SCOPE model's RTMo program to calculate interactions between the canopy surface and the atmosphere, as well as the solar and sky irradiance spectra (Verhoef et al., 2018). These atmospheric parameters were then integrated with canopy reflectance and SIF signals as outlined in Equation 1.~~ Atmospheric radiative transfer functions were derived from the Moderate-resolution Atmospheric TRANsmission model (MODTRAN5; Berk et al., 1998, 2000) to generate TOA radiance. Critical processing steps included: (1) using the MODTRAN Interrogation Technique (MIT) (Verhoef and Bach, 2012; Verhoef et al., 2018) to extract 18 spectral transfer functions parameterized by aerosol optical depth, water vapor content, and observation geometry from MODTRAN5 outputs; (2) using the RTMo module in SCOPE, which dynamically couples these functions with bidirectional reflectance distribution (BRDF) and SIF emission spectra to resolve surface-atmosphere interactions. The simulated atmospheric parameters, canopy reflectance, and SIF signals were then integrated using the radiative transfer operator defined in Equation 1 to generate the TOA radiance spectra across the 640–850 nm range.

For the original MODTRAN 5 dataset, SR and SSI are approximately 0.005 nm. To simulate satellite observations, the original spectral data underwent convolution and resampling techniques tailored to the specific SR and SSI of various bands, as detailed in Table 3. Based on the configuration of the TanSat-2 satellite, we established two spectral channels with distinct spectral ranges. The spectral response functions were modeled using Gaussian functions, which correlate with the SR (Zhao et al., 2022b; Zou et al., 2022). This modeling process employs a filter kernel, K, defined by both the original and adjusted SR levels, to convolve the initial 0.005 nm spectrum into the new spectral resolution. Consequently, the radiance for a given wavelength (λ) is calculated using the following equations (Damm et al., 2011; Zou et al., 2022):

$$L_{TOA} \approx \frac{\int_{\lambda-\varepsilon}^{\lambda+\varepsilon} L_{TOA}(\hat{\lambda}) \cdot K(\lambda-\hat{\lambda}) d\hat{\lambda}}{\int_{\lambda-\varepsilon}^{\lambda+\varepsilon} K(\lambda-\hat{\lambda}) d\hat{\lambda}} \quad (2)$$

$$K(\lambda-\hat{\lambda}) = \frac{2\sqrt{2ln2}}{\sqrt{2\pi}\sqrt{SR_d^2-SR_o^2}} \cdot \exp\left(-\frac{4(ln2)(\lambda-\hat{\lambda})^2}{SR_d^2-SR_o^2}\right) \quad (3)$$

where λ represents the center wavelength after undergoing spectral sampling, while $\hat{\lambda}$ corresponds to the wavelength in the original dataset. $L_{TOA}(\hat{\lambda})$ denotes the TOA radiance output by MODTRAN and SCOPE simulations. The term SR_o refers to the initial spectral resolution (0.005 nm), and SR_d corresponds to the spectral resolution relevant to the various channels. The parameter ε, indicating the kernel's half-width in wavelength terms, was set to three times SR_d. For computational efficiency, a summation

approach was utilized in lieu of direct integration, with the differential wavelength interval, $d\hat{\lambda}$, fixed at 0.005 nm. This process involved resampling the original spectra by selecting wavelength points (λ) at intervals defined by the SSI for each channel, ensuring adequate coverage within the sensor's spectral coverage (SC).

Finally, random noise was incorporated into the data, quantified by the SNR, which varies with both radiance levels and wavelength (Köhler et al., 2015; Zou et al., 2022).

$$SNR(Rad, \lambda) = SNR_{ref}\sqrt{\frac{Rad(\lambda)}{Rad_{ref}}} \quad (4)$$

where SNR_{ref} represents the reference SNR at the reference radiance level Rad_{ref}.

2.2.2 Spectral simulation dataset

In the context of vegetative scenes, a total of 1008 cases were examined, incorporating combinations of diverse leaf biochemical characteristics, canopy structures, and geometric conditions, as illustrated in Table 4. For non- vegetation targets, ten distinct reflectance spectra representing snow and bare soil surfaces were sourced from the Image Visualization Environment (ENVI) spectral library (Clark and Swayze, 1995). A total of 1280 atmospheric and observational conditions were simulated (Table 4), with the observational conditions aligning with those of the SCOPE model. Ultimately, 12,800 non-vegetated spectra and 161,280 vegetative spectra were generated as training and test datasets.

Table 4. Input parameters used in the MODTRAN and SCOPE.

Parameters of MODTRAN5	Value
Atmospheric temperature profile	Middle latitude summer/winter
Aerosol optical thickness at 550 nm	0.05, 0.12, 0.2, 0.3, 0.4
Vertical water vapor column (g cm^{-2})	0.5, 1.5, 2.5, 4
Surface altitude (km)	0.01, 0.05, 1, 2
Solar zenith angle (degree)	15, 30, 45, 70
View zenith angle (degree)	0, 16
Parameters of SCOPE	**Value**
Leaf area index (LAI)	0.5, 1, 2, 3, 4, 5, 7
Fluorescence quantum efficiency (fqe)	0.01, 0.02, 0.04
Chlorophyll content (Cab) (ug cm^{-2})	20, 30, 40, 50, 60, 80
Solar zenith angle (degree)	15, 30, 45,70
View zenith angle (degree)	0, 16

Fig. 1 presents the simulated spectrum with an SR of 0.12 nm and an SSI of 0.04 nm. The displayed solar-induced fluorescence (SIF) spectra exhibit characteristic double peaks in the red and far-red bands, around 685 nm and 740 nm, respectively. Additionally, the spectra distinctly reveal the absorption features of the Earth's atmosphere, as well as the Fraunhofer lines.

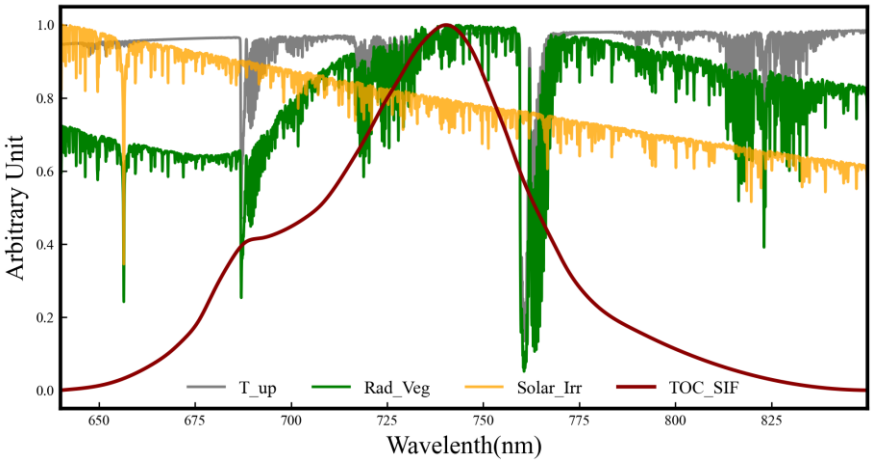

Figure 1. A collective set of normalized, simulated spectra at the TOA over vegetated surfaces (Rad_Veg), together with the incident solar radiance that arrives at the TOC (Solar_Irr), upward transmittance of the atmosphere (T_up), and SIF at the TOC (TOC_SIF). These spectra are presented with an SR of 0.12 nm and an SSI of 0.04 nm derived from SCOPE and MODTRAN 5 models.

2.2.3 End-to-end orbit simulation dataset

TanSat-2 boasts a spatial resolution of 2 km paired with a swath width of 2,900 km, enabling it to offer high spatio-temporal resolution and comprehensive observations. Its expansive swath ensures nearly global coverage each day. Utilizing the J2 orbit perturbation model and TanSat-2's orbital elements, we simulated its orbit—a critically inclined, sun-synchronous trajectory. This simulation facilitated the assessment of global surface observations to model the worldwide spatiotemporal distribution of data collected by TanSat-2. Under typical acquisition scenarios, global simulations were conducted, harnessing the satellite's spatiotemporal resolution to simulate the TOA radiance spectra received by TanSat-2. The aim is to explore the spatiotemporal capabilities of TanSat-2 in retrieving SIF from its global observations.

For our study, mid-June was selected due to the peak greenness of vegetation in the Northern Hemisphere, which corresponds with the greatest global variability in vegetation cover. The end-to-end simulation of TOA radiance, in line with Equation 1 and following the spectral simulation process described in Section 2.2.2, combined the SCOPE and MODTRAN models to generate the reflectance and SIF spectra, as well as atmospheric functions. Limitations in globally representative data for vegetation and atmospheric parameters introduce some discrepancies in the end-to-end simulation processes compared to the spectral simulation, as depicted in Fig. 2.

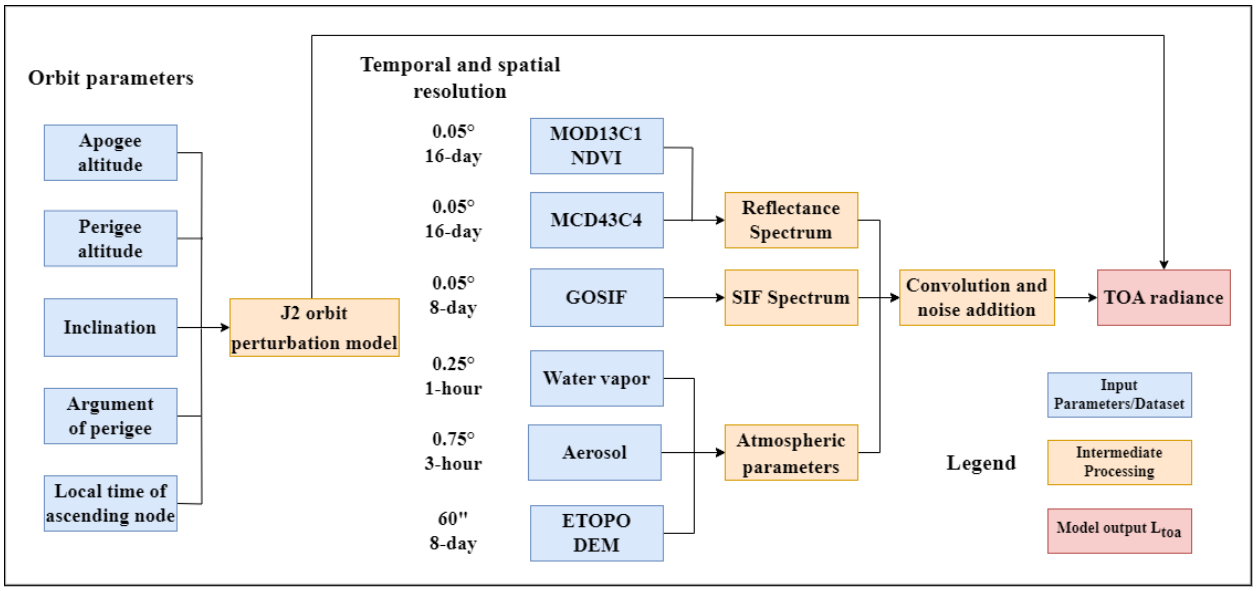

Figure 2. Flowchart of the end-to-end orbit simulations.

~~Reflectance spectra calculations utilized the green, red, and near-infrared bands from the Moderate Resolution Imaging Spectroradiometer (MODIS) MCD43C4 product (Huete et al., 2002). To accurately reflect real-world conditions, different simulation strategies for vegetation and non-vegetation surfaces were implemented. Global screening employed NDVI data from the MODIS MOD13C1 product (Huete et al., 2002), using a threshold of 0.2 to differentiate between non-green and green vegetation. Non-vegetation reflectance spectra were fitted using quadratic polynomials. Meanwhile, vegetation reflectance spectra, due to their complexity in these bands, were simulated using the data from Section 2.1. A singular value decomposition (SVD) was performed, and the first two basis vectors were extracted to fit the spectral data, as illustrated in Fig. 3, with interpolation across the 640-800 nm range. For SIF spectra, the global OCO-2 SIF dataset (GOSIF) (Li et al., 2018) was used to map the global SIF distribution, filling data gaps through interpolation and depicting SIF spectral shape with a typical profile shown in Fig. 1.~~

The spectral reflectance characterization leveraged multi-band observations from the Moderate Resolution Imaging Spectroradiometer (MODIS) MCD43C4 product (Huete et al., 2002), incorporating green (555 nm), red (659 nm), and near-infrared (858 nm) spectral bands. To account for surface heterogeneity, distinct spectral simulation approaches were developed for vegetated and non-vegetated surfaces. Vegetation coverage was delineated using the MODIS MOD13C1 Normalized Difference Vegetation Index (NDVI) product (Huete et al., 2002), with a NDVI threshold of 0.2 discriminating non-photosynthetic vegetation from active canopies.

Non-vegetated surface reflectance spectra were parameterized through quadratic polynomial fitting, while vegetation spectra required advanced spectral decomposition due to their complex radiative interactions. As demonstrated in Fig. 3, vegetation reflectance characteristics between 640-800 nm were reconstructed through singular value decomposition (SVD) of the reference spectra described in Section 2.1, retaining the first two orthogonal basis vectors that collectively explained >95% of spectral variance. SIF spatial patterns were derived from the global OCO-2-based SIF product (GOSIF v2, Li et al., 2018), with spectral continuity achieved through adaptive gap-filling interpolation and depicting SIF spectral shape with a typical profile shown in Fig. 1.

~~Datasets representing the global distribution of atmospheric conditions were assembled, incorporating water vapor data sourced from the ERA5, the fifth generation reanalysis of global climate and weather by the European Centre for Medium-Range Weather Forecasts (ECMWF) (Hersbach et al., 2020), and aerosol information from ECMWF's Atmospheric Composition Reanalysis 4 (EAC4), provided by the Copernicus Atmosphere Monitoring Service (CAMS) (Inness et al., 2019). Additionally, the 60-arcsecond~~

~~resolution DEM data from Earth TOPOgraphy (ETOPO), furnished by the National Oceanic and Atmospheric Administration (NOAA) (Amante and Eakins, 2009), was resampled to a spatial resolution of 0.02 degrees to align with the satellite payload specifications. To accommodate the atmospheric conditions data, we expanded the range of atmospheric parameters outlined in Table 4, with further details provided in Table 5. These data are essential for calculating parameters such as ρ_0, S, $T_{\downarrow\uparrow}$, and $T_{\uparrow}$ in Equation 1, which are crucial for simulating TOA radiance. To optimize simulation times, we eschewed the use of MODTRAN 5 for per-pixel atmospheric parameter simulation, opting instead for a random forest model. We sampled 10% of the atmospheric conditions from Table 5—a total of 7,680 data points—and input them into MODTRAN 5 to simulate key atmospheric parameters. These parameters were then used to train the random forest model, which was subsequently employed to simulate the atmospheric parameters for each pixel. These simulations were incorporated into Equation 1 to compute TOA radiance. Additional processes, including convolution and noise addition, were applied. Figure 4 illustrates a pseudo-color image synthesized using the near-infrared, red, and green bands of MCD43C4, displaying the fitted reflectance and TOA radiances across seven representative geomorphic areas.~~

The atmospheric parameterization framework was constructed using a synthesis of global datasets to characterize key environmental variables. Total column water vapor data were obtained from ERA5 (the fifth generation ECMWF reanalysis; Hersbach et al., 2020), while aerosol information was acquired from the EAC4 reanalysis (Copernicus Atmosphere Monitoring Service; Inness et al., 2019). Topographic elevation data were derived from the ETOPO digital elevation model (NOAA; Amante and Eakins, 2009). Atmospheric temperature profiles were partitioned according to latitude. The atmospheric parameter space outlined in Table 4 was expanded (see Table 5) to compute critical radiative transfer variables (ρ_0, S, $T_{\downarrow\uparrow}$, and $T_{\uparrow}$ in Equation 1) required for simulating TOA radiance. To address computational constraints associated with full-resolution MODTRAN 5 radiative transfer modeling, a machine learning surrogate strategy was implemented. A representative subset of 7,680 atmospheric scenarios (10% of parameter combinations in Table 5) was simulated using MODTRAN 5. These simulations trained a random forest regressor to predict atmospheric parameters across the global domain at 0.02° resolution. These simulations were incorporated into Equation 1 to compute TOA radiance. Additional processes, including convolution and noise addition, were applied.

It should be noted that we did not explicitly simulate cloud contamination or utilize cloud cover products for screening purposes. As such, our end-to-end orbital simulation operates under the assumption of clear sky conditions, deliberately excluding the potential impacts of cloud cover. Furthermore, the CAPHI instrument aboard the satellite will supply data on AOD and cloud coverage, enhancing our understanding of atmospheric conditions and cloud dynamics, while also providing supplementary data for future SIF retrieval efforts with TanSat-2. Furthermore, our simulations exclude rotational Raman scattering (RRS) effects. The RRS effects will be relatively small in the spectral range of red and far-red band (Vasilkov et al., 2013). Fig. 4 presents pseudo-color composites using the near-infrared, red, and green bands of MCD43C4, comparing surface reflectance reconstructions with simulated TOA radiances in seven geomorphologically distinct regions, including desert, boreal forest, and tropical rainforest ecosystems.

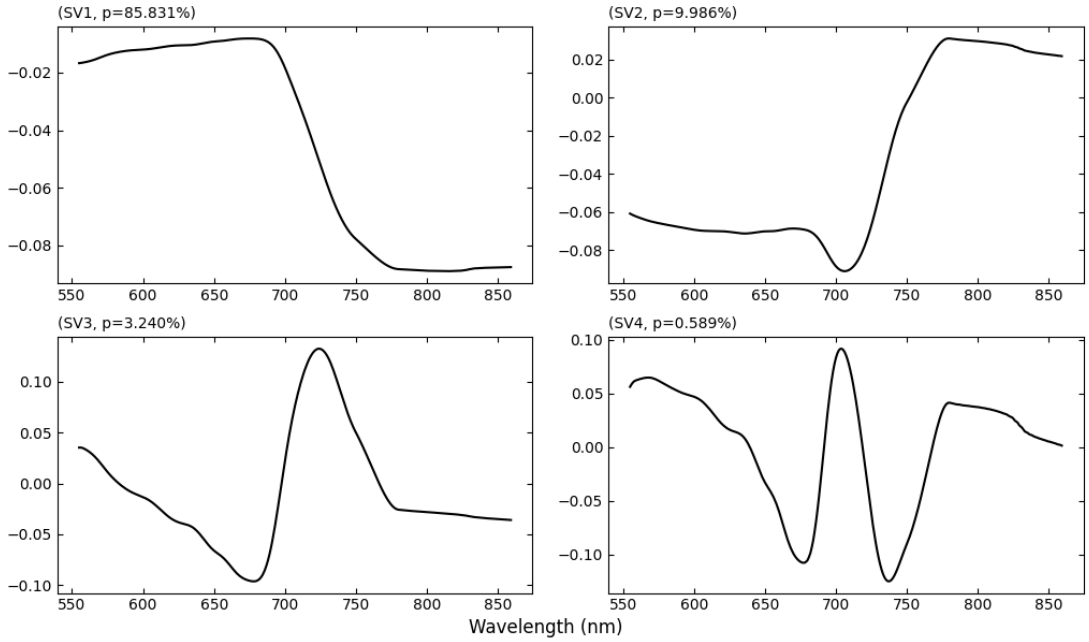

Figure 3. The first four singular vectors from the singular value decomposition of the reflectance training dataset.

Table 5. Look-up table (LUT) of MODTRAN 5 used to train the atmospheric parameter random forest model

Parameters of MODTRAN5	Value
Atmospheric temperature profile	Tropical, middle latitude summer/winter, subarctic summer/winter
Aerosol optical thickness at 550 nm	0.05, 0.12, 0.2, 0.3, 0.4, 0.6, 1.0, 2.0, 3.0, 4.0
Vertical water vapor column (g cm^{-2})	0.5, 1.5, 2.5, 4.0, 6.0, 8.0
Surface altitude (km)	0.01, 0.05, 1, 2, 3, 4, 5, 6
Solar zenith angle (degree)	15, 22, 30, 37, 45, 52, 60, 70
View zenith angle (degree)	0, 8, 16, 25

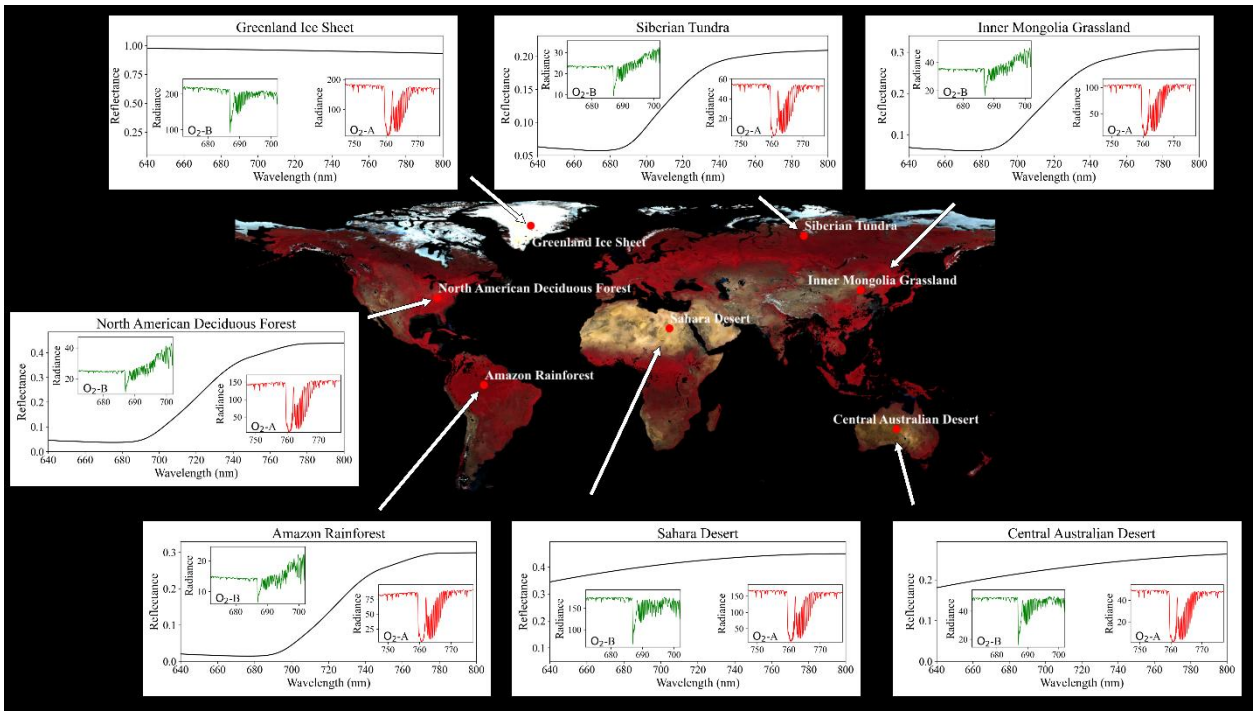

Figure 4. Global reflectance pseudo-color composite and the BOA reflectance along with simulated TOA radiance for two channels in typical regions.

Moreover, we adopted strategies similar to those utilized by Du et al. (2018) to create datasets as training samples for the data-driven method. Our selection criteria targeted non-vegetation surfaces, such as bare soil and snow, to minimize biases and uncertainties. The SZA and view zenith angle (VZA) were restricted to less than 75° and 60°, respectively, ensuring that the SZA within the training dataset were representative. We used the MODIS MCD43C4 BRDF-adjusted reflectance product to identify non-vegetation surfaces. As demonstrated by Guanter et al. (2012), the criterion RNIR < RSWIR effectively differentiates bare soil from other surface types. Bright soil pixels, characterized by high reflectivity, were identified using the MODIS data, specifically when the reflectance in band 6 surpassed that in band 2 and exceeded a threshold value of 0.2. Additionally, snow-covered areas were delineated employing the Normalized Difference Snow Index (NDSI) as defined by Salomonson and Appel (2004). A pixel was identified as snow-covered when its NDSI value exceeded 0.4, with further constraints on reflectance values in the near-infrared (band 2) above 0.11 and in band 4 above 0.10, following the criteria established by Riggs et al. (2006).

To ensure the training dataset's representativeness and variability, spectra were selected to be uniformly distributed across the globe. Consequently, 400,000 spectra were randomly sampled to achieve this diversity.

3 Retrieval method for TanSat-2 simulation dataset

3.1 Data-Driven SIF Retrieval Algorithm

SVD technology, akin to Principal Component Analysis, is extensively utilized for solving linear equations and is pivotal in statistical analysis and reducing dimensionality in large datasets (Du et al., 2018). In models driven by data, the initial segment of Equation 1, which excludes fluorescence effects, integrates high-frequency and low-frequency components. As delineated by Guanter et al. (2012, 2013), high-frequency components, stemming from atmospheric absorption influenced by solar and terrestrial sources, are extracted from non-vegetation datasets through SVD and reconstructed using a select set of characteristic spectra. Conversely, the low-frequency components, representing atmospheric scattering (denoted as ρ_0 and S) and surface reflectance (ρ_s),

are approximated using polynomial wavelength functions (λ). Moreover, the shape of SIF spectra is typically modeled through a normalized Gaussian function (h_f).

$$h_f = \exp\left(-\left[\frac{-(\lambda-\lambda_0)^2}{2\sigma_h^2}\right]\right) \quad (5)$$

where λ_0 is the peak emission wavelength of SIF spectral in the far-red and red bands, and the value of σ_h determines the shape of SIF spectral. Therefore, equation (1) can be rewritten as:

$$L_{TOA} = v_1 \cdot \sum_{j=0}^{n_p}\left(\beta_j \lambda^j\right) + \sum_{k=2}^{n_v}(\gamma_k v_k) + F_s \cdot h_f \cdot T_\uparrow^e \quad (6)$$

where β and γ represent the coefficients vectors to be determined, n_p is the polynomial order, v refers to the singular vectors of the high-frequency components, with their number given by n_v. $T_\uparrow^e$ is the effective upward transmittance to represent the atmospheric transmittance from the surface to the sensor. $T_\uparrow^e$ can be estimated before retrieval (Köhler et al., 2015):

$$T_\uparrow^e = exp\left[lnT_{\downarrow\uparrow}^e \cdot \frac{\sec(\theta_v)}{\sec(\theta_0)+\sec(\theta_v)}\right] \quad (7)$$

where $T_{\downarrow\uparrow}^e$ represents the effective two-way atmospheric transmittance, obtained by normalizing the TOA reflectance using low-order polynomials. θ_0 and θ_v is the SZA and VZA, respectively.

~~For spectral characterization of SIF, the parameters λ_0 and σ_h for the far red band are set at 740 nm and 21 nm, respectively. The red band utilizes a combination of two Gaussian functions to depict a more intricate spectral shape, with λ_0 being 740 nm and 685 nm, and σ_h being 21 nm and 10 nm, respectively (Joiner et al., 2016; Zou et al., 2022). This spectral region encapsulates numerous solar Fraunhofer lines and atmospheric absorption features, enhancing the retrieval capabilities of SIF. Specifically, the spectral domain of TanSat-2 encompasses absorption lines such as the O_2-A at 758-772 nm and the O_2-B at 682-692 nm, which are integral for retrieving far red and red SIF, respectively (Joiner et al., 2013; Guanter et al., 2015). Surrounding solar Fraunhofer and atmospheric absorption lines also play a crucial role in the SIF retrieval process in satellites with refined spectral resolution (Frankenberg et al., 2011; Joiner et al., 2011). As part of a semi-empirical approach, the performance of data-driven algorithms heavily relies on the empirical parameters used in the model. To optimize these parameters, different window settings were applied for each channel. The window settings for the far-red band were 747-758 nm, 759-772 nm, and 747-777 nm; for the red band, they were 672-686 nm, 682-697 nm, and 672-702 nm. Moreover, the permissible ranges for the parameters n_p (0-7) and n_v (1-50) were established for SIF retrieval (Köhler et al., 2015; Zou et al., 2022). Ultimately, only the parameters a_i, β_j, γ_k, and F_S remained as variables, with F_S determined through resolving the linear least squares problem.~~ The spectral parameterization of SIF employed Gaussian functions with band-specific configurations. For the far-red band, a single Gaussian function was adopted with λ_0 of 740 nm and σ_h of 21 nm. The red band required a dual Gaussian representation to capture its complex spectral features, characterized by λ_0 values of 685 nm and 740 nm with corresponding σ_h values of 10 nm and 21 nm, respectively (Joiner et al., 2016; Zou et al., 2022). These spectral regions encompass critical atmospheric absorption bands—specifically, the O_2-A band (758–772 nm) for far-red SIF and the O_2-B band (682–692 nm) for red SIF retrieval (Guanter et al., 2015; Joiner et al., 2013). Surrounding solar Fraunhofer and atmospheric absorption lines also play a crucial role in the SIF retrieval process in satellites with refined spectral resolution (Frankenberg et al., 2011; Joiner et al., 2011).

As a semi-empirical approach, the performance of data-driven algorithms heavily depends on the empirical parameters employed in the model. To optimize these parameters, different retrieval windows were selected for each channel. Specifically, the far-red band employed window settings of 747–758 nm, 759–772 nm, and 747–777 nm, while the red band used 672–686 nm, 682–697 nm, and 672–702 nm. Additionally, the permissible ranges for the parameters n_p (0–7) and n_v (1–50) were defined for SIF retrieval (Köhler et al., 2015; Zou et al., 2022). Through variable reduction, the final retrievals retained only β_j, γ_k, and F_s, resolved via linear least squares optimization.

~~SVD efficiently transforms a large set of correlated variables into a streamlined set of uncorrelated components, known as singular vectors. These vectors are strategically arranged such that each successive vector accounts for progressively less signal variability, enabling a hierarchical representation of data. By leveraging the principal singular vectors, we can reconstruct similar signals and effectively filter out noise. The implementation of SVD was carried out on the training dataset from spectral simulations. Figure 5 illustrates the first six basis vectors for two distinct channels. Each subplot also quantifies the explained variance associated with each basis vector in the simulations. Predominantly, the spectral variations within the fitting window arise from Fraunhofer lines and atmospheric absorption features. It is evident that the initial set of singular vectors encapsulates the majority of the spectral variance across all simulations, while none of the vectors correspond to the SIF spectral shape.~~ SVD was applied to spectral simulation datasets to disentangle dominant signal components from noise. These vectors are strategically arranged such that each successive vector accounts for progressively less signal variability, enabling a hierarchical representation of data. The first six basis vectors accounted for over 98% of cumulative spectral variance, as quantified in Fig. 5. Predominantly, the spectral variations within the fitting window arise from Fraunhofer lines and atmospheric absorption features. Notably, none of the basis vectors exhibited correlation with intrinsic SIF spectral shapes, confirming the method's capability to isolate fluorescence signals from background radiative processes.

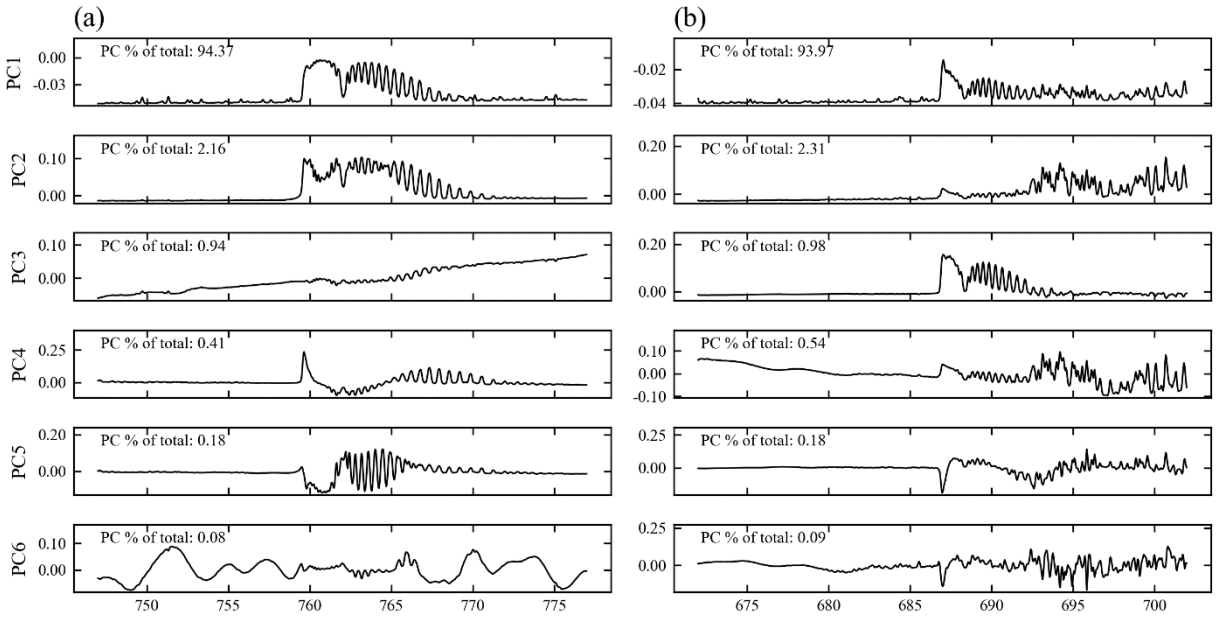

Figure 5. The first 6 bias vectors from the SVD of the spectral simulation training dataset in two spectral ranges: (a) 747–777 nm and (b) 672–702 nm.

3.2 Metrics for Evaluating Accuracy

For the simulated SIF intensities at 740 nm and 685 nm, we designated these values as the true SIF signals (SIF_{true}) for each channel, respectively. To evaluate the accuracy of the spectral retrieval, we compared the retrieved SIF values ($SIF_{retrieved}$) at these wavelengths with SIF_{true}. The analysis included calculating the root-mean-squared error (RMSE) to quantify the retrieval precision. Additionally, several statistical metrics were employed to further assess the retrieval performance, such as the slope and intercept from the linear regression between $SIF_{retrieved}$ and SIF_{true}, alongside the coefficient of determination (R^2). The adjusted SIF values (SIF_{corr}), intended to rectify systematic biases inherent in data-driven retrieval methods, were computed as per Equation (8) (Du et al., 2020; Zou et al., 2022).

$$SIF_{corr} = \frac{SIF_{retrieved} - intercept}{slope} \quad (8)$$

where the intercept and slope represent the parameters of the linear relationship between $SIF_{retrieved}$ and SIF_{true}, expressed as $SIF_{retrieved} = SIF_{true} \times slope + intercept$. The corrected RMSE (RMSE*) was calculated by comparing SIF_{true} with SIF_{corr}.

3.3 Quality filtering rules for global SIF composites

Global composites of SIF were generated by averaging retrieval data across a grid with a resolution of 0.05° by 0.05° over a 1-day period. Before averaging, the retrieval data underwent a filtering process based on established quality criteria (Du et al., 2018; Guanter et al., 2021). The criteria include:

(1) Land surface.

(2) SZA of <70° and the VZA of <60°.

(3) χ^2_{red} estimates inside the 95% range of expected values.

where Chi-square (χ^2) test is a statistical method used to evaluate how well a model fits observed data by measuring the difference between observed and fitted data. If the fitted radiances deviate significantly from the observed radiances, it indicates a poor fit. The reduced Chi-square (χ^2_{red}) is calculated by dividing the Chi-square value by the degrees of freedom.

4 Results

4.1 Optimization of empirical parameters in the data-driven algorithm using spectral simulations

4.1.1 Impact of empirical parameters on SIF retrievals

To refine the parameterization of the algorithm that guides the TanSat-2 SIF retrieval, we have conducted a quantitative analysis based on spectral simulations. This study evaluates the impact of various empirical parameters utilized in data-driven algorithms on the retrieval outcomes. Parameters investigated include the configuration of the fitting windows, the number of eigenvectors (n_v), and the polynomial order (n_p).

In our analysis, we implemented differing window settings across two spectral channels, as depicted in Fig. 6. A comparative analysis reveals substantial variations in retrieval performance among the window settings. Notably, the optimal retrieval windows for both channels exclusively utilized atmospheric windows for retrieval, achieving root mean square errors (RMSEs) of 0.24 and 0.19 mW m^{-2} sr^{-1} nm^{-1}, respectively. Wider fitting windows tend to encompass atmospheric absorption bands, offering a plethora of usable spectral data. However, this approach necessitates precise simulation of atmospheric upwelling transmittance and complicates the modeling of vegetation surface reflectance and SIF spectral shape, particularly in the red band. Consequently, a narrower atmospheric window band frequently serves as a more advantageous choice for the spectral parameters of TanSat-2.

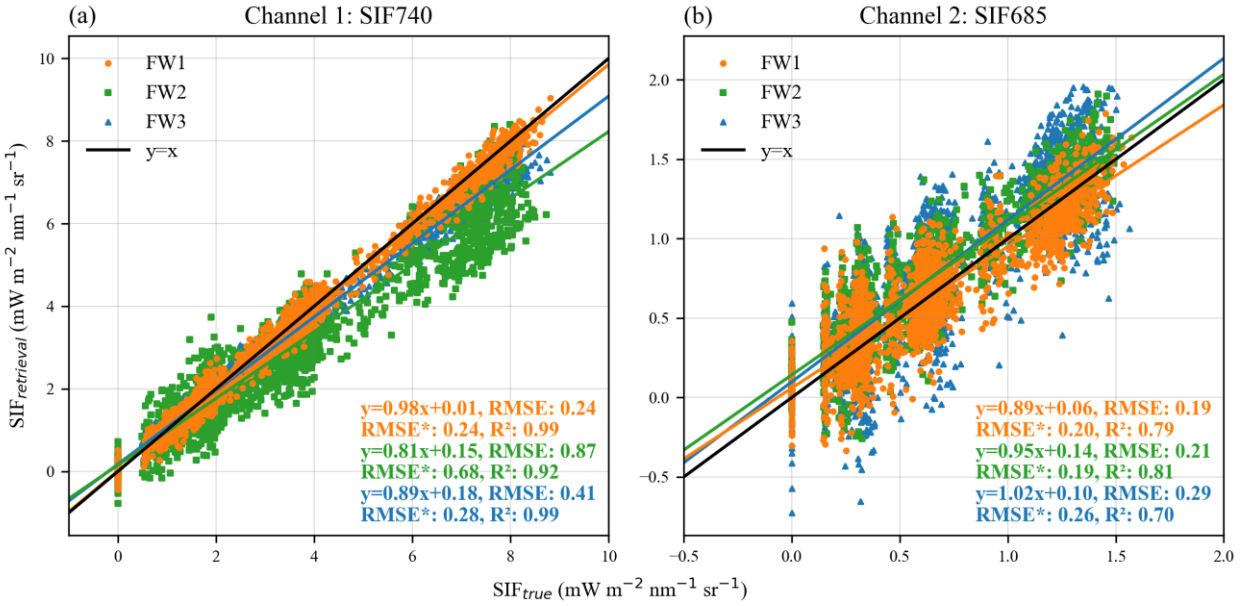

Figure 6. Retrieval using simulated datasets of two channels with different fitting windows: the windows for channel 1 are 747-758 nm, 759-772 nm, and 747-777 nm; the windows for channel 2 are 672-686 nm, 682-697 nm, and 672-702 nm. For demonstration purposes, only a randomly selected portion of the data is used to draw the scatter plot.

The relationship between the number of eigenvectors and RMSEs was examined within the context of the optimal fitting window, as illustrated in Fig. 7. The analysis indicates that RMSEs initially decrease, subsequently increase, and ultimately stabilize as the number of eigenvectors grows. Optimal n_v values were determined to be 6 for channel 1 and 4 for channel 2.

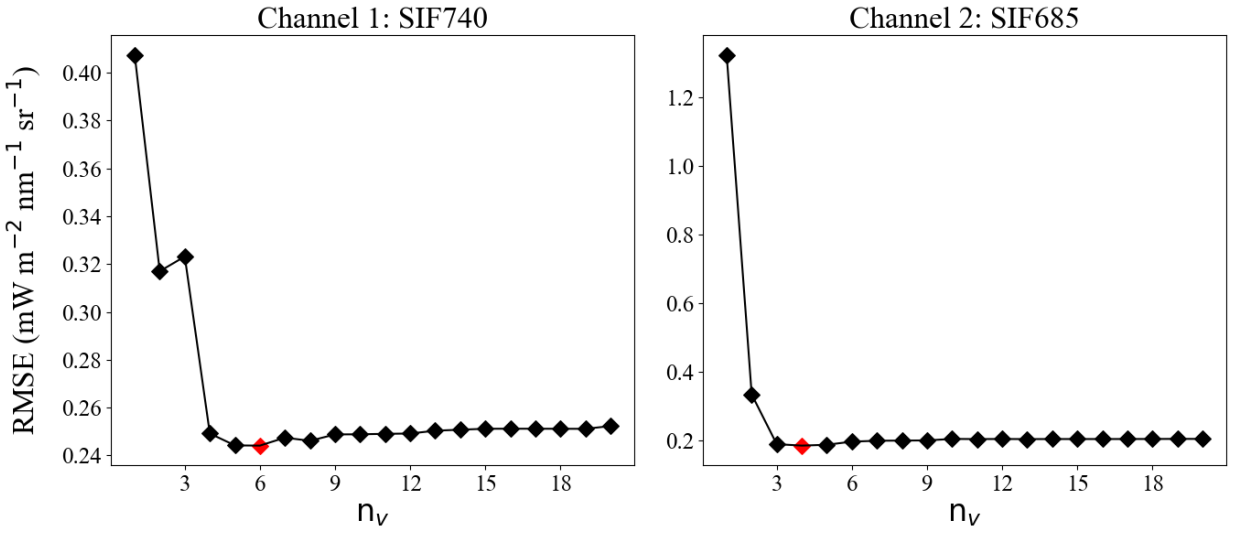

Figure 7. RMSE of SIF retrieval in the optimal fitting windows using varying numbers of eigenvectors. The red point refers to the optimal n_v.

Data-driven models commonly employ polynomials to approximate the shape of reflectance and atmospheric scattering within the fitting window. Typically, a broader fitting window necessitates the use of higher-order polynomials. The red band, positioned near the vegetation's red edge and heavily influenced by chlorophyll absorption, exhibits notably complex reflectance patterns. Thus, higher polynomial orders are generally required for the red band compared to the far-red band. An analysis utilizing the optimal window revealed that RMSE values initially decrease and then increase with the escalation of polynomial order, as detailed in Fig. 8. This pattern arises because low polynomial orders fail to accurately model the reflectance spectral shape, whereas

excessively high orders induce overfitting, obstructing the detection of faint SIF signals within the upstream radiance. After surpassing a certain threshold, RMSE stabilizes at a high value. For channels 1 and 2, the optimal polynomial orders were found to be 2 and 4, respectively.

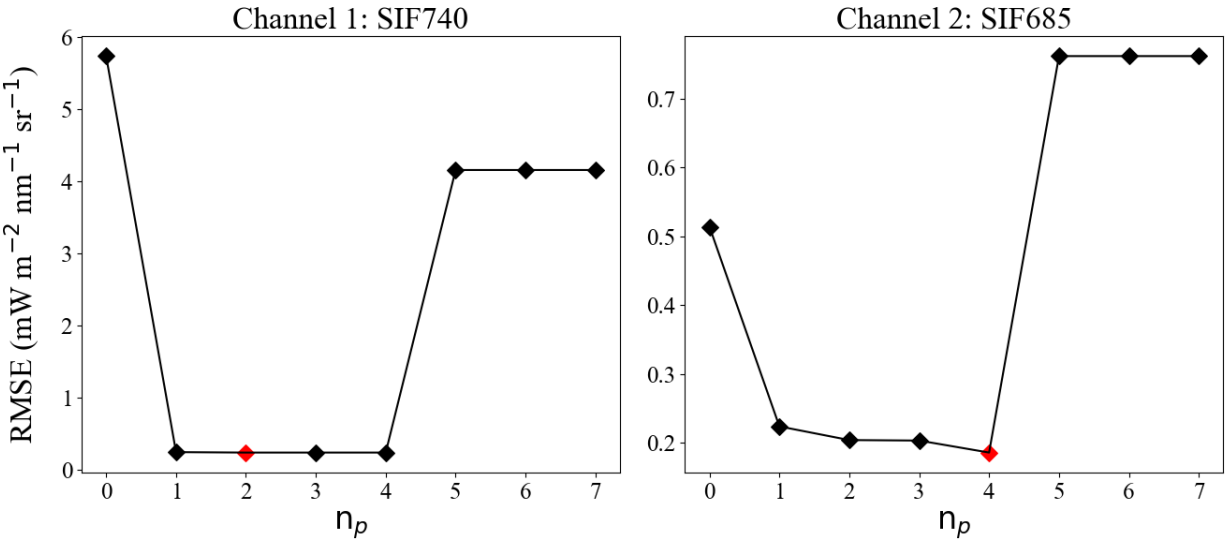

Figure 8. RMSE of SIF retrieval in the optimal fitting windows using a varying polynomial order. The red point refers to the optimal n_p.

4.1.2 SIF retrievals using optimized empirical parameters

SIF retrieval was performed using the spectral simulation of the TanSat-2 payload configuration to evaluate its retrieval potential. We assessed the retrieved SIF values ($SIF_{retrieval}$) against the actual values (SIF_{true}) under varied atmospheric conditions, leaf biochemical characteristics, canopy structure, and geometrical arrangements. The results presented in Fig. 9 illustrate the SIF retrievals for TanSat-2, utilizing the optimally derived empirical parameters.

For the two spectral channels examined, the scatter plot distributions align closely with the 1:1 line, indicating high retrieval accuracy. In channel 1, the data-driven algorithm was optimized with settings that included a spectral fitting window from 747–758 nm, a second-order polynomial fitting, and six eigenvectors, yielding an RMSE of 0.24 mW m^{-2} sr^{-1} nm^{-1}. Channel 2 employed a fourth-order polynomial and four eigenvectors within a 672–686 nm window, achieving an RMSE of 0.19 mW m^{-2} sr^{-1} nm^{-1}. Furthermore, the correlation between the RMSE and its normalized counterpart (RMSE*) suggests minimal systematic errors in the retrieval methodology.

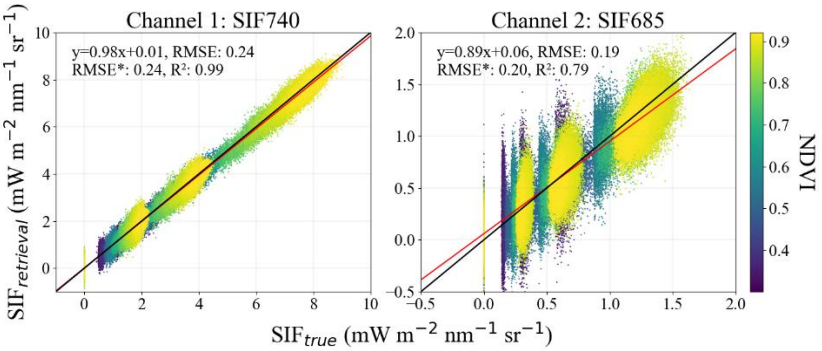

Figure 9. SIF retrievals of spectral simulation using two channels with optimal parameter settings. The black line denotes 'y = x', while the red one denotes the linear fitting line.

To illustrate the forward model fit, TOA radiance spectra for the ranges 747–758 nm and 672–686 nm were simulated using both the standard forward model and a variant excluding SIF. Comparison of these spectra against actual TOA radiance measurements yielded two spectral residuals, depicted in Fig. 10. Models incorporating SIF showed significantly lower spectral residuals, particularly around the Fraunhofer lines. Additionally, in the forward model that includes SIF, the spectral residuals across both channels were generally minimal, underlining the efficacy of the SVD method in fitting data and accurately reconstructing surface spectral shapes absent of SIF signals.

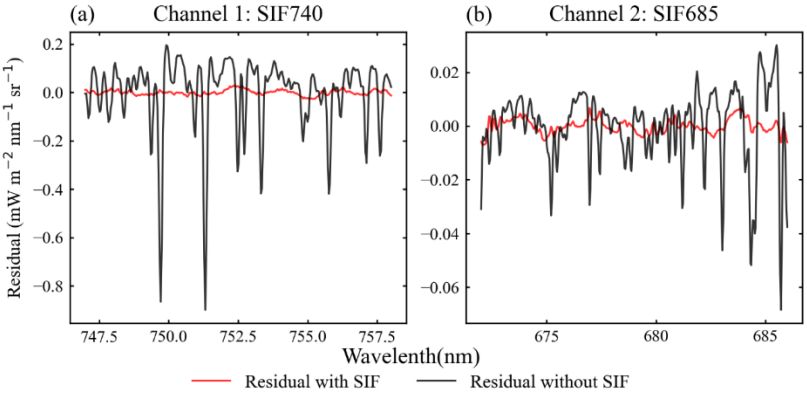

Figure 10. Spectral residuals between the fitted and observed TOA radiances, shown for cases where the model includes SIF (red) and excludes SIF (black) in two spectral ranges: (a) 747–758 nm and (b) 672–686 nm. (a) and (b) correspond to channels 1 and 2.

4.2 Evaluation of SIF retrievals based on end-to-end orbit simulations

In Section 4.1, we evaluated the impact of empirical parameters on SIF retrieval accuracy using a data-driven model and established an optimal algorithm for the two channels on TanSat-2, based on spectral simulations detailed in Section 2.2.2. This section also discusses how retrieval errors from a single pass of TanSat-2 propagate into the spatiotemporal composite. Fig. 11 illustrates the global distribution of observations measured by TanSat-2 within a 0.05° global grid over a single day. Despite the fine resolution, the satellite's high spatial resolution and wide swath enabled a substantial volume of observations, approximately 5-7 times greater than that achieved by TROPOMI. These payload characteristics of TanSat-2 significantly enhance the reliability of SIF retrievals.

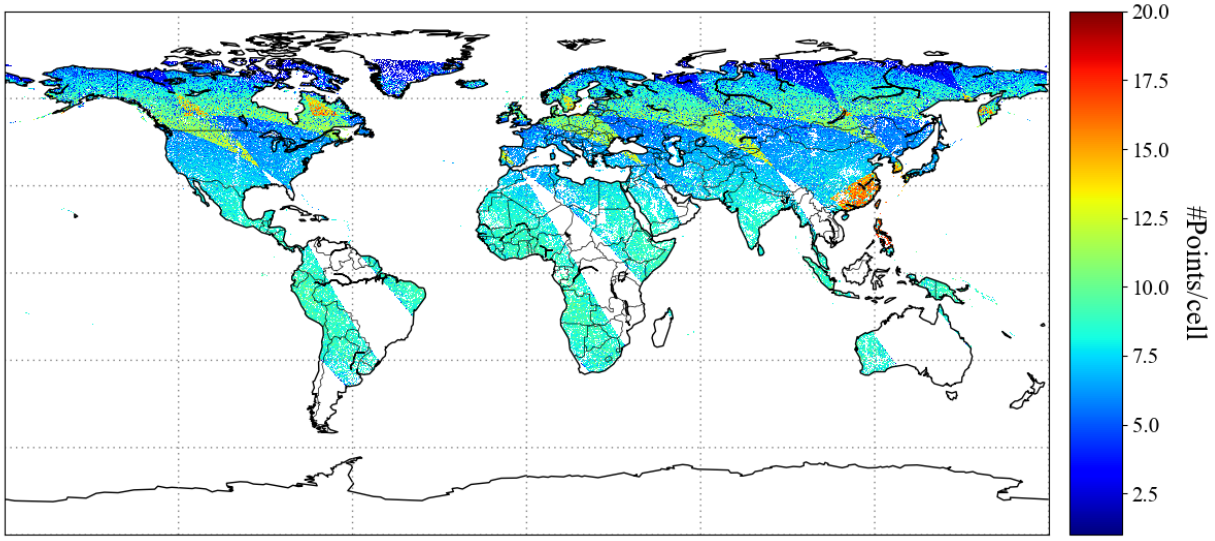

Figure 11. Global map showing the total number of TanSat-2 observations. The simulations represent daily averages for June, with a grid resolution of 0.05°.

The aggregated SIF retrieval results for two bands and the global observations of SIF (GOSIF) over a 1-day period, displayed in Fig. 12 with a grid size of 0.05°, demonstrate a strong correlation. High SIF values are noted in densely vegetated regions, with the highest global SIF signals occurring in the eastern United States. Conversely, SIF values near zero are observed in regions such as Greenland, the Sahara Desert, and much of Australia. For the analysis, GOSIF values at 757 nm were converted to 740 nm and 685 nm to represent the actual SIF of the two channels. This conversion involved multiplying the 757 nm SIF values by factors of 1.48 and 0.54, respectively, which align with the SIF spectral shape used in the end-to-end orbit simulated dataset (refer to Fig. 1). A comparison of the retrieved SIF with the true SIF shows discrepancies generally less than 0.15 mW m^{-2} sr^{-1} nm^{-1}, as illustrated in Fig. 13. The R^2 values for the two channels are 0.88 and 0.61, respectively, with corresponding RMSE values of 0.082 and 0.061. These RMSE values represent approximately 5.4% and 11.1% of the globally observed SIF peaks, which are considered acceptable error thresholds for SIF synthesis (Fig. 14).

The retrieval uncertainties manifest predominantly as spectrally structured noise coupled with pronounced sensitivity to atmospheric scattering processes. The former primarily varies with scene-specific radiance magnitudes within retrieval windows, while systematic SIF underestimation in high aerosol-loading regimes arises from unaccounted scattering effects within our forward model. In order to disentangle the error sources, we conducted a statistical analysis of the far-red SIF retrieval errors (results for the red band are similar) in relation to AOD, the albedo within the fitting window, SZA, and VZA, as shown in Fig. 15. The results indicate that RMSE increases significantly with the increase in surface albedo and the decrease in SZA. Both changes enhance the background radiance, leading to a noticeable rise in retrieval uncertainty due to an increase in signal noise. Spatially, these retrieval errors dominate in bright surface areas, such as the Sahara Desert and the Congo Basin, as shown in Fig. 13. Meanwhile, retrieval bias exhibits substantial amplification under higher AOD and larger VZA. This phenomenon arises because the higher AOD strengthens atmospheric scattering efficiency, while larger VZA values extend the effective radiative path length. These factors collectively amplify atmospheric scattering effects, resulting in progressively larger underestimation of SIF. The spatial pattern of this bias prominently features regions with high aerosol, particularly Central and South Asia, as depicted in Fig. 13. Notably, red-SIF retrieval over aquatic environments necessitates distinct processing techniques compared to terrestrial environments. This technical disparity manifests as substantially exaggerated SIF estimates within specific watersheds, particularly those in northern/western Russia and the Great Lakes region of North America.

~~Moreover, we evaluated the results for 4-day and 8-day composites, shown in Figs. A2 and A4. As the number of observations increases, R^2 improves significantly, while RMSE decreases, further demonstrating the instrument's performance onboard the TanSat-2 satellite. It should be noted that although the AOD product used partially accounts for cloud impacts, it does not explicitly model cloud contamination or apply cloud fraction products for screening. Consequently, the results in Figs. 12–14 assume clear-sky conditions. Additionally, these simulations do not incorporate rotational Raman scattering (RRS), as the filter only considers data with a solar zenith angle (SZA) less than 75°, where the RRS effect is expected to be minimal.~~

Moreover, we evaluated the results of 4-day and 8-day composites, as shown in Fig. A1 and A2. Compared to single-day observations, the global coverage is more comprehensive, and the composite method significantly reduces retrieval errors by increasing observation density and suppressing noise (the RMSE for the 4-day and 8-day composites decreased by 35% and 47%, respectively). This further demonstrates the performance of the instrument on the TanSat-2 satellite. However, several persistent systematic biases were detected: underestimation in high AOD regions (Central Asia/South Asia) due to enhanced atmospheric scattering, overestimation in bright surfaces (Sahara Desert, Congo Basin) caused by radiation saturation, and overestimation of red SIF near water bodies (Russian rivers, Great Lakes in North America) due to residual surface reflectance effects. Overall, the 4-day and 8-day composites achieved excellent accuracy, demonstrating robust retrieval performance that balances spatial coverage and accuracy. The R^2 values for the two channels were 0.95 and 0.79, and 0.97 and 0.85, respectively, while the RMSE values

were 0.053 and 0.041, and 0.043 and 0.034 mW m^{-2} sr^{-1} nm^{-1}. It should be noted that although the AOD product used partially accounts for cloud impacts, it does not explicitly model cloud contamination or apply cloud fraction products for screening. Consequently, our results assume clear-sky conditions. Additionally, these simulations do not incorporate RRS, as the filter only considers data with a SZA less than 70°, where the RRS effects are minimal.

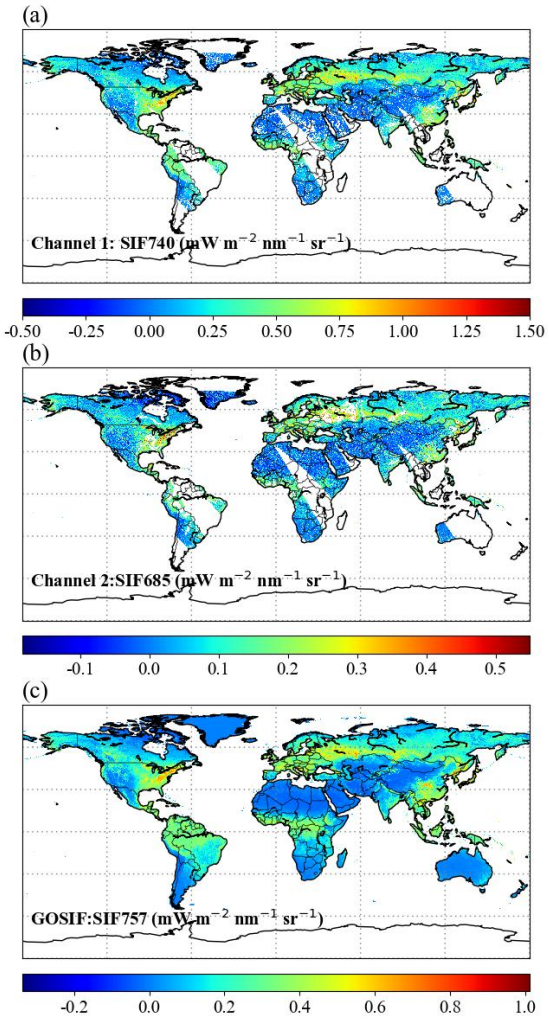

Figure 12. Global maps of mean SIF for each of the two channels, with GOSIF serving as the reference for true SIF, under the same conditions as Fig. 11. The SIF range is scaled according to the proportion of the SIF spectrum used.

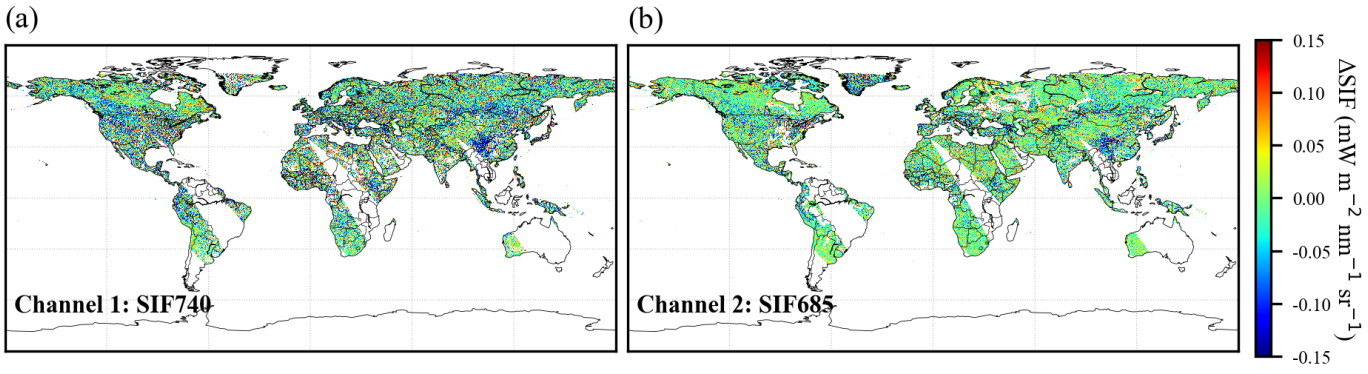

Figure 13. SIF retrieval errors (ΔSIF = retrieved SIF - true SIF) for two channels, under the same conditions as Fig. 11.

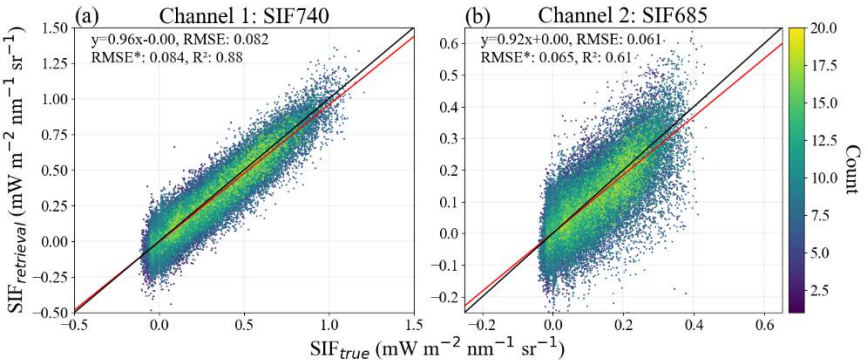

Figure 14. Global simulations of SIF retrieval from two channels, under the same conditions as Fig. 11. The black line denotes 'y = x', while the red one denotes the linear fitting line.

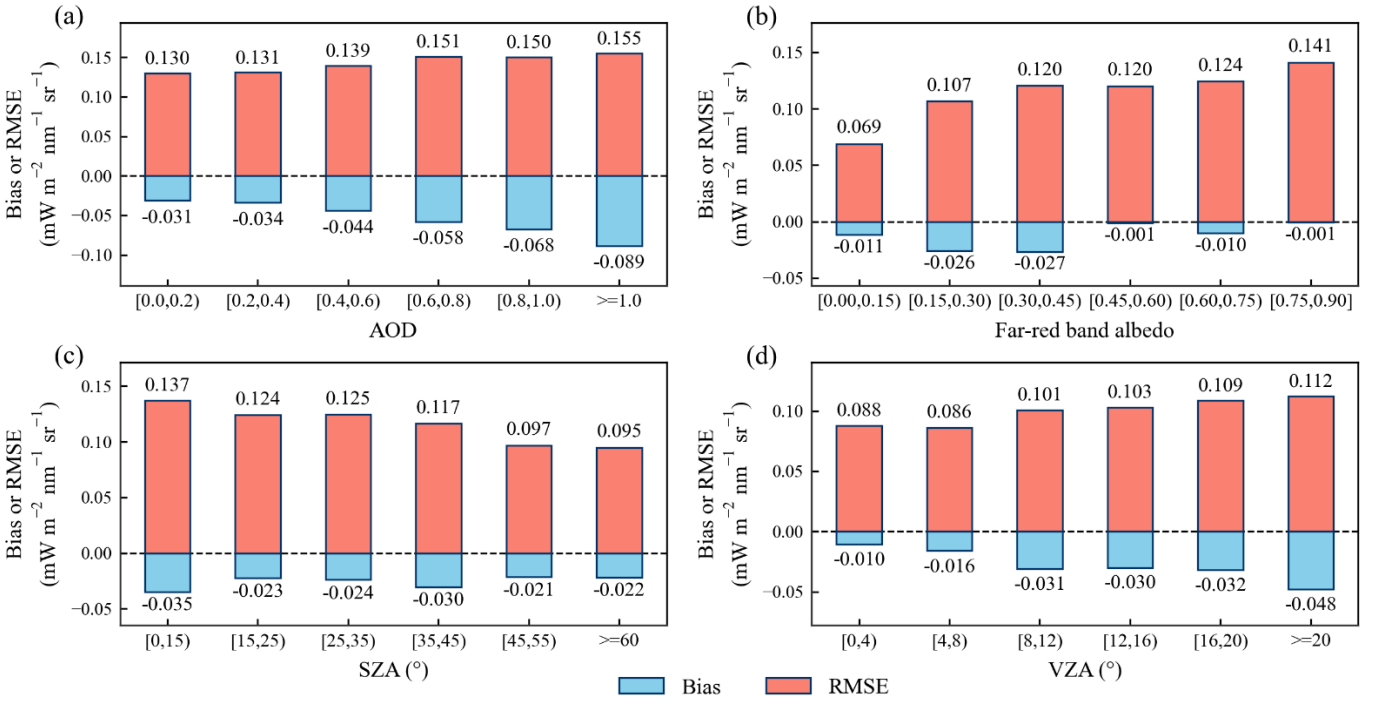

Figure 15. Statistical analysis of far-red SIF retrieval errors with respect to (a) AOD, (b) far-red band albedo, (c) SZA, and (d) VZA. The bias represents the mean value of ΔSIF (retrieved SIF - true SIF).

5 Discussion

5.1 Representativeness of simulations to satellite observations

~~For the end-to-end orbit simulation, we modeled TanSat-2's Earth observations based on its orbital parameters, using data from various sources to represent the global distribution of surface reflectance, SIF, and atmospheric conditions.~~ For the end-to-end orbit simulation, we modeled TanSat-2's Earth observations based on its orbital parameters. Designed to optimize global carbon stocktaking, the inclined elliptical orbit enhances observational frequency over the Northern Hemisphere's densely populated regions (e.g., Asia, North America, and Europe), as evidenced by the increased observation density shown in Fig. 11 and Fig. A1. Continuous observations over four- or eight-day cycles ensure near-global coverage. However, this orbital architecture introduces

inherent challenges. The efficiency of the sun-synchronous elliptical orbit is relatively low, as its apogee is approximately ten times higher than its perigee. Although the imaging setting only allow observation for orbital altitudes above ~2,350 km, significant altitude disparity still persists. This results in a swath width variation exceeding twofold, leading to uneven ground coverage and spatial resolution, which in turn reduces the efficiency of achieving uniform global sampling—particularly in equatorial regions. Furthermore, the orbit may induce field of view aberrations that could compromise measurement accuracy. These limitations necessitate systematic mitigation strategies during satellite system design and orbital parameter optimization.

In this study, we used data from various sources to represent the global distribution of surface reflectance, SIF, and atmospheric conditions. Although the simulation is driven by satellite datasets, it cannot fully capture the complexities present in actual satellite measurements, such as instrument artifacts or RRS effects. In the simulation, radiances are initially generated monochromatically through scattering, and then convolved with the instrument response function. The instrument response function is modeled using a Gaussian profile. For simulating random noise, a simplified SNR model (Equation 4) was applied. Zou et al. (2022) compared the simulated spectra and SNR with actual satellite measurements, and the results demonstrated high consistency between the two, validating the accuracy of the SNR model and the spectral filtering process. Thus, it is feasible to assess the SIF retrieval capability of TanSat-2 based on the simulated dataset.

Additionally, while the AOD dataset partially incorporates the influence of clouds—particularly in areas of high value—we did not explicitly simulate cloud contamination or utilize cloud cover products for screening purposes. The satellite's observations inherently reflect the impact of clouds on the radiance signal. The establishment of various cloud screening criteria involves a trade-off between mitigating the clear-sky bias inherent in satellite observations and optimizing the accuracy of SIF retrieval (Frankenberg et al., 2014b). Stringent cloud screening measures can lead to a reduction in the overall number of usable measurements, consequently producing a noisier output map. This paper aims to investigate the benefits derived from the TanSat-2 sensor's superior spectral observation capabilities and its high temporal and spatial resolution in SIF retrieval. As such, our end-to-end orbital simulation operates under the assumption of clear sky conditions, deliberately excluding the potential impacts of cloud cover. Furthermore, the CAPHI instrument aboard the satellite will supply data on AOD and cloud coverage, enhancing our understanding of atmospheric conditions and cloud dynamics, while also providing supplementary data for future SIF retrieval efforts with TanSat-2.

It should be noted that our simulations did not account for radiative effects induced by RRS. The RRS intensity typically decreases with increasing wavelength (Vasilkov et al., 2013), and its spectral interference is statistically negligible within the red to far-red spectral bands. Moreover, the data-driven SIF retrieval framework inherently addresses potential RRS contamination through basis vector parameterization (Joiner et al., 2016). This approach enables the decoupling of RRS-induced spectral variations from SIF emission signals.

5.2 Advancing global vegetation dynamics insights through TanSat-2 observations

The TanSat-2 mission is equipped with a SIF imaging spectrometer that continuously gathers high spectral resolution data across the O_2-A and O_2-B bands, boasting excellent SNR. The precise retrieval of red and far-red SIF is vital for advancing our comprehension of plant photosynthesis and global carbon cycles. Moreover, the satellite’s wide-swath and high spatial resolution capabilities promise significant improvements in the informational content of SIF data, especially in regions characterized by fragmented vegetation, thereby facilitating more frequent and valid observations.

The integration of SIF signals from distinct spectral bands offers unique advantages for monitoring vegetation health and photosynthesis (Liu et al., 2017). Notably, the majority of SIF emissions stem from photosystem II (PSII) protein complexes involved in photosynthesis, whereas photosystem I (PSI) predominantly contributes to far-red fluorescence, with its influence

increasing at longer wavelengths and typically remaining unaffected by biochemical factors. In contrast, the contributions from PSII are modulated by physiological regulation, leaf structure, and chemical composition (Verrelst et al., 2015). Ač et al. (2015) conducted a meta-analysis that concluded canopy-level red and far-red SIF diminishes under water stress, while the ratio of red to far-red fluorescence increases in response to nitrogen deficiency. Red and far-red SIF can serve as early indicators of both water stress and recovery (Daumard et al., 2010; Xu et al., 2018). By utilizing high-precision spectral data from TanSat-2 for dual-band SIF retrieval, the capacity to detect vegetation physiological parameters is significantly enhanced, offering substantial advantages for monitoring vegetation health. Furthermore, Verrelst et al. (2015) demonstrated that peaks in red SIF emission are strongly influenced by carboxylation capacity (Vcmo), which correlates with photosynthetic capacity. Consequently, employing dual-band emission fluxes, rather than relying solely on a single far-red band, proves more effective for correlating SIF with photosynthetic metrics such as gross primary productivity (GPP).

6 Conclusion

The TanSat-2 satellite is specifically designed for global carbon inventory verification. It features a wide swath of 2900 km and high spatial resolution of 2 km at an orbit altitude of 7000 km, providing near-daily global baseline coverage. Additionally, it is equipped with a wide spectral range and high spectral specifications, enabling dual-band SIF retrievals with unprecedented accuracy. This paper employs spectral simulations to optimize empirical parameters for data-driven SIF retrieval in two channels of the TanSat-2 satellite. Using the optimized data-driven algorithm, the RMSEs of SIF retrievals for the two channels are 0.24 m and 0.19 mW m^{-2} sr^{-1} nm^{-1}, respectively. Furthermore, the potential of the forthcoming TanSat-2 satellite for global SIF monitoring is evaluated through end-to-end simulations at a global scale. Comparisons between daily and 0.05° global composites of dual-band SIF retrievals and GOSIF indicate strong agreement, with R^2 values of 0.88 and 0.61, and RMSE values of 0.082 and 0.061 mW m^{-2} sr^{-1} nm^{-1} for the SIF retrievals at the two bands. Therefore, TanSat-2 presents significant opportunities for SIF retrieval at both red and far-red bands, offering high resolution, precision, and frequency of coverage, which is crucial for a comprehensive understanding of global vegetation photosynthetic activities and the terrestrial carbon cycle.

Appendix A

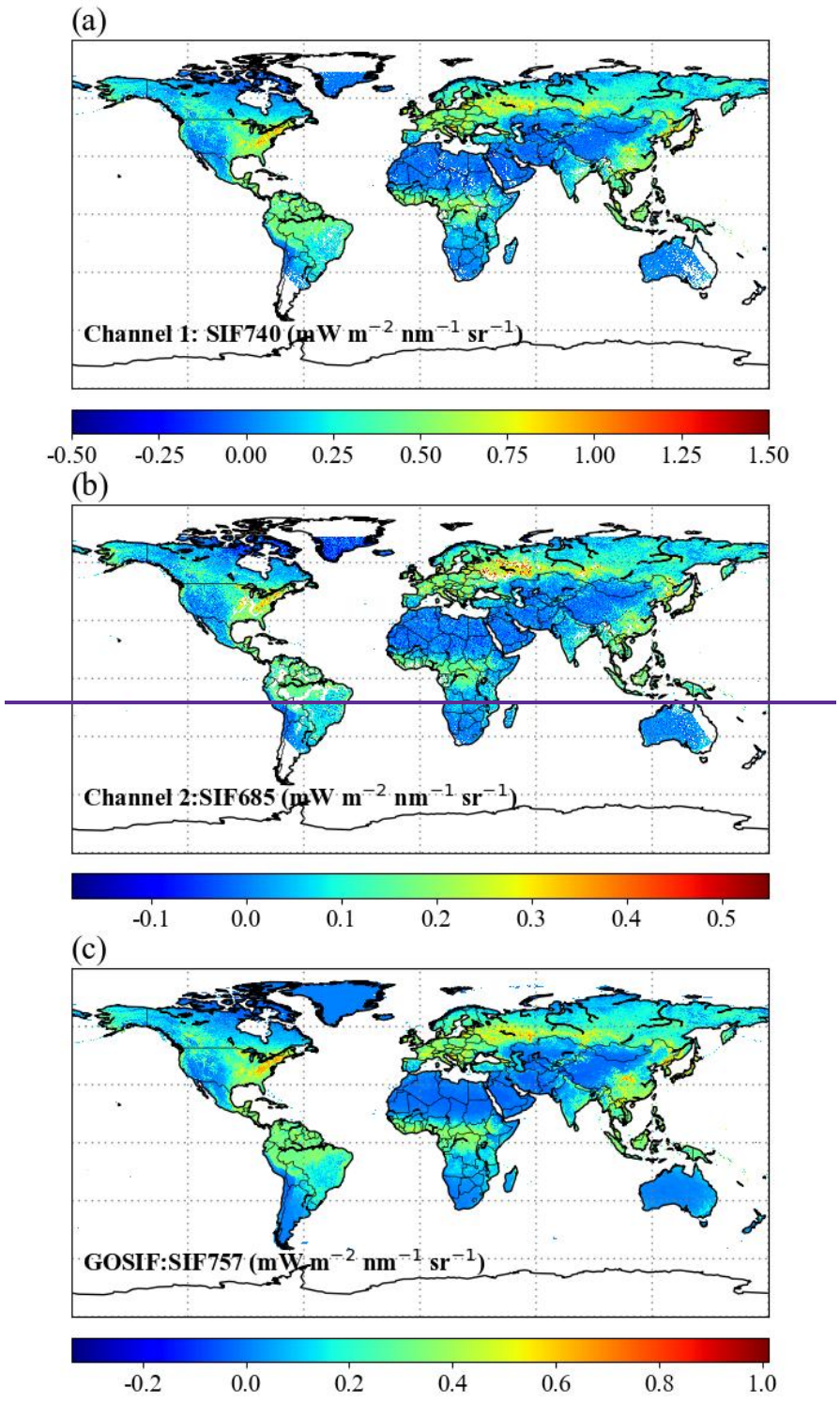

~~**Figure A1.** Global maps of mean SIF for each of the two channels, with GOSIF serving as the reference for true SIF. The SIF range is scaled according to the proportion of the SIF spectrum used. The simulations represent 4-day time averages for June.~~

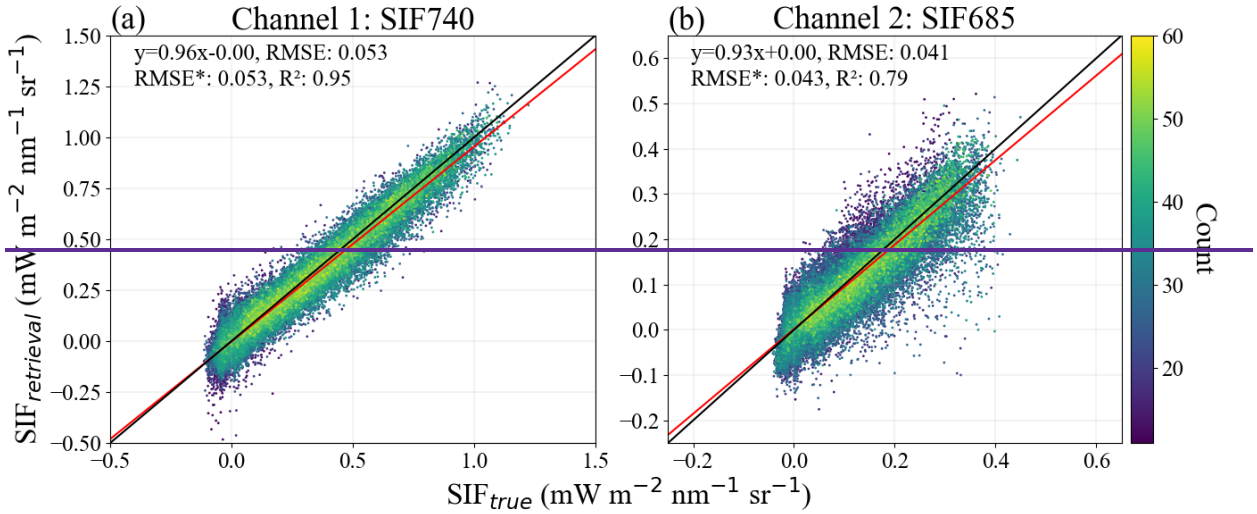

Figure A2. Global simulations of SIF retrieval from two channels, under the same conditions as Fig. A1. The black line denotes 'y = x', while the red one denotes the linear fitting line.

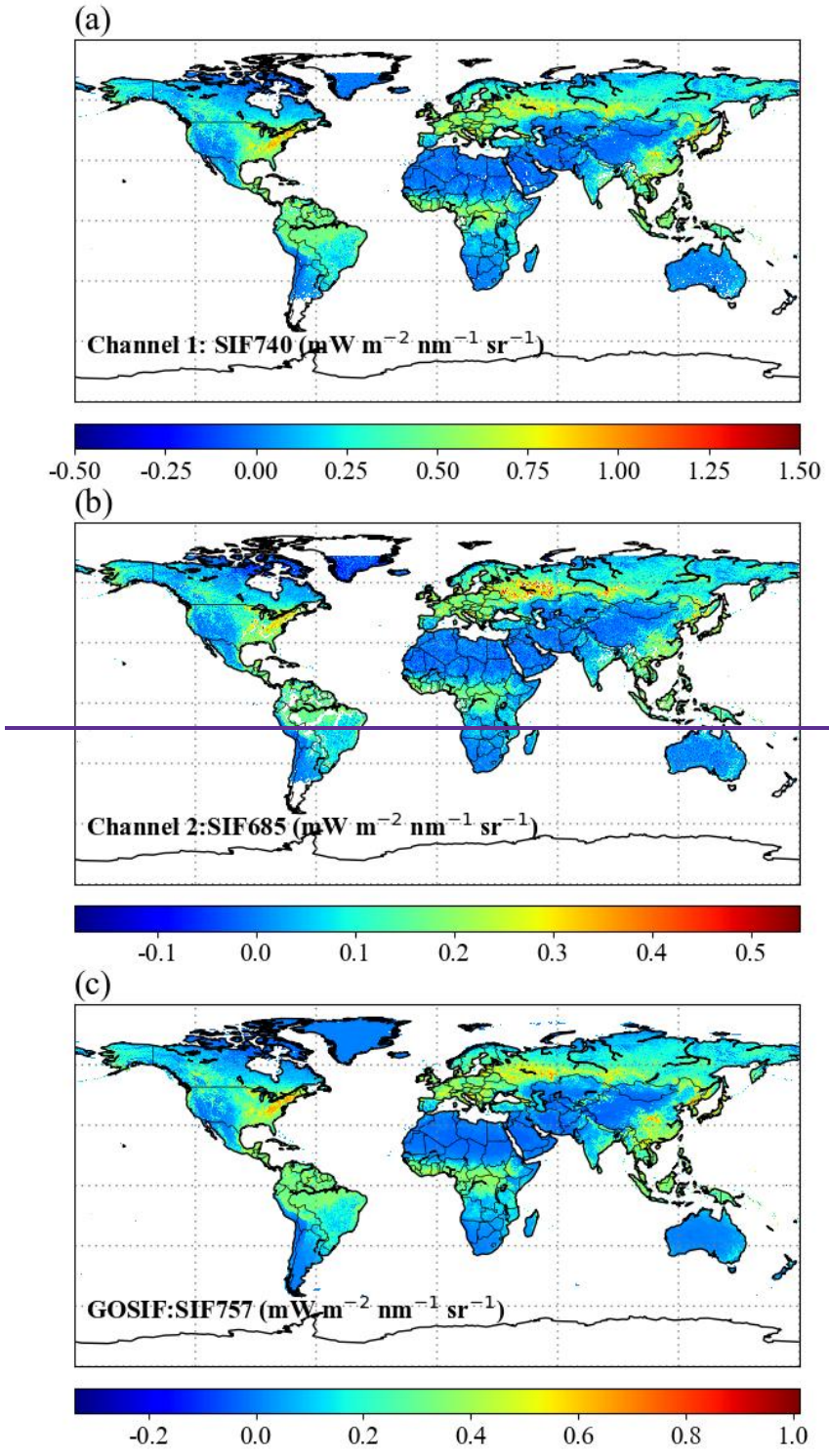

Figure A3. Global maps of mean SIF for each of the two channels, with GOSIF serving as the reference for true SIF. The SIF range is scaled according to the proportion of the SIF spectrum utilized. The simulations represent 8-day averages for June.

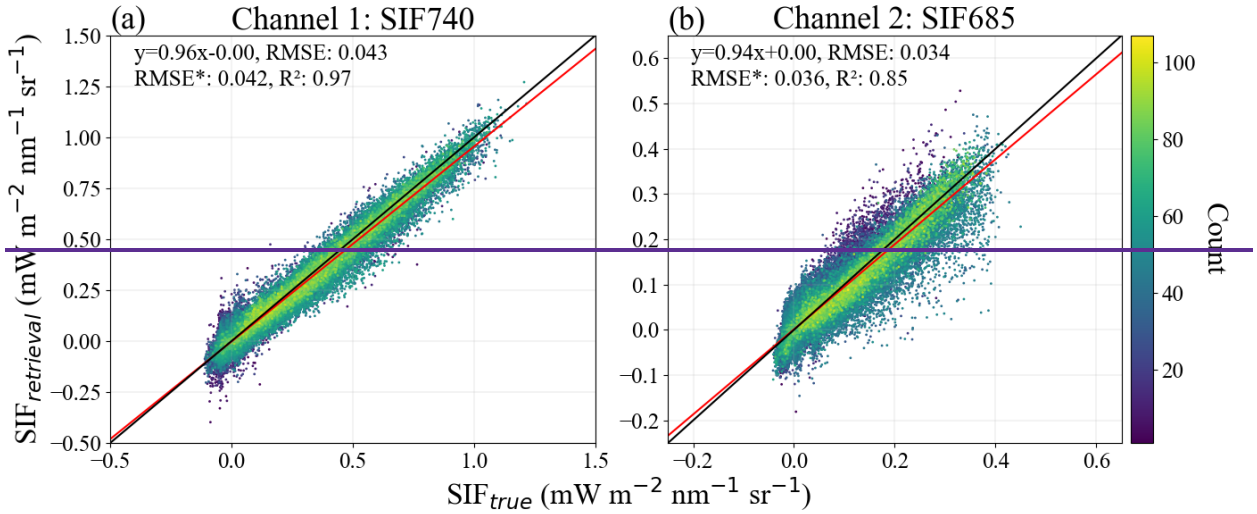

~~Figure A4.~~ ~~Global simulations of SIF retrieval from two channels, under the same conditions as Fig. A3. The black line denotes 'y = x', while the red one denotes the linear fitting line.~~

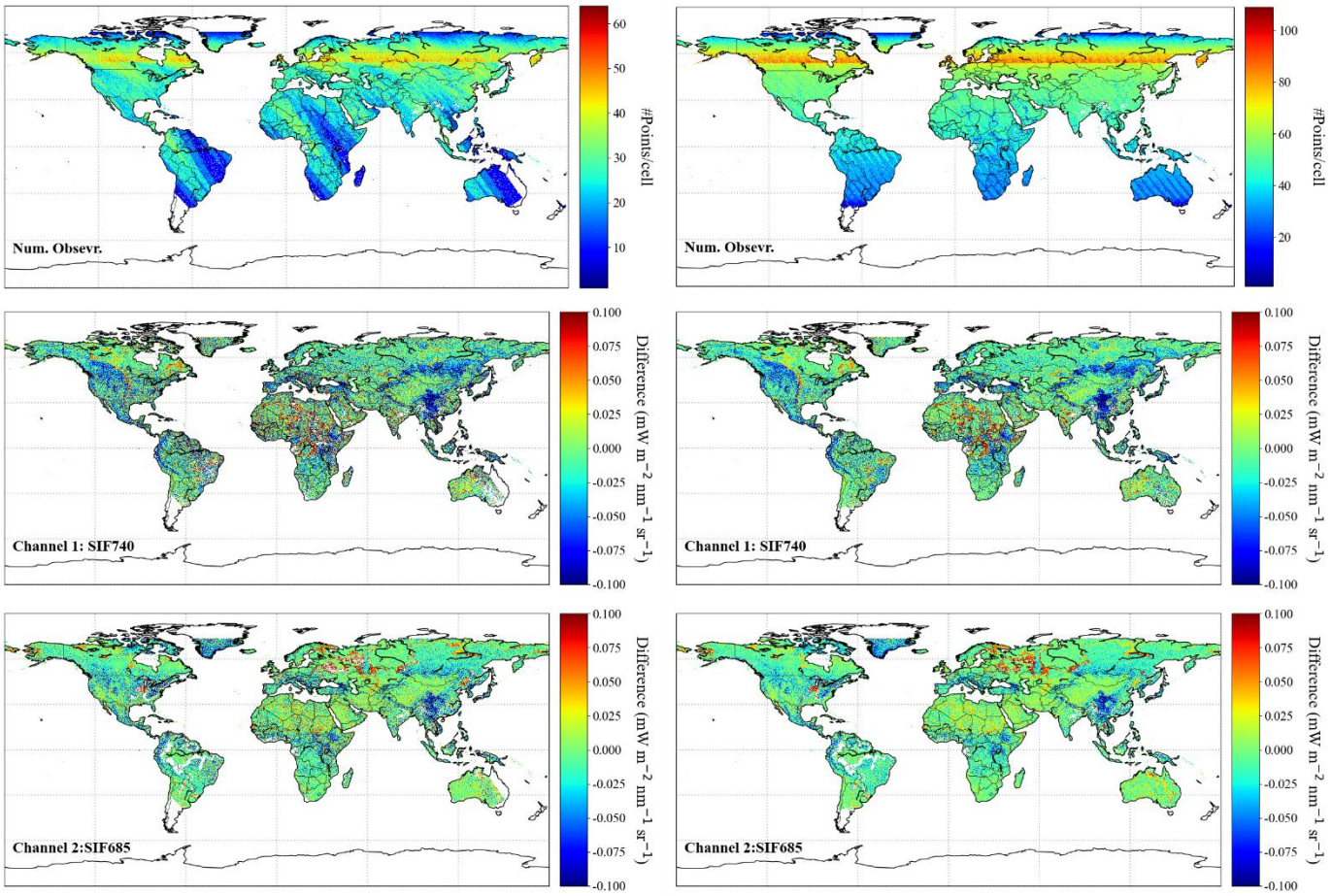

Figure A1. Global maps of TanSat-2 observation counts (top panels) and retrieval errors (retrieved SIF minus reference SIF) for Channel 1 (middle panels) and Channel 2 (bottom panels). Results derive from 4-day (left column) and 8-day (right column) composites at 0.05° grid resolution.

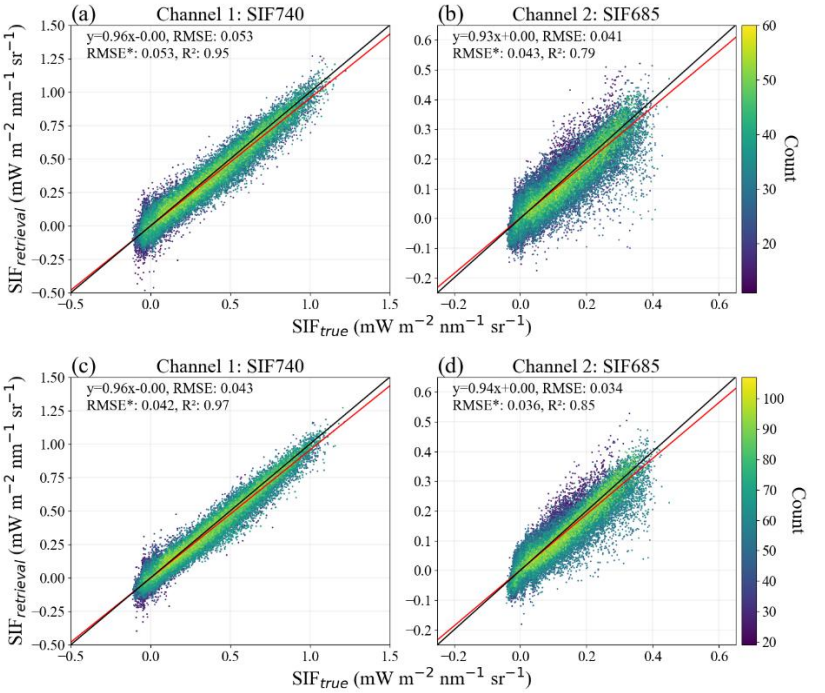

Figure A2. Retrieved versus reference SIF relationships for TanSat-2's two channels derived from 4-day composites (a, b) and 8-day composites (c, d). Black lines denote the 1:1 relationship, while red lines indicate linear regression fits.

585

Author contributions. DZ, SD, and LL designed the experiments and DZ carried them out. DZ developed the model code and prepared the manuscript. CZ, MF, and YD contributed significantly to the research method and the manuscript revision. LT provided important support concerning the descriptions of the satellite.

590 *Competing interests.* The authors declare no conflicts of interest

Financial support. This work was funded by the National Key Research and Development Program Earth Observation and Navigation Key Project (grant no. 2023YFB3907405) and the National Natural Science Foundation of China (grant no. 42201356).

Reference

Ač, A., Malenovský, Z., Olejníčková, J., Gallé, A., Rascher, U., and Mohammed, G.: Meta-analysis assessing potential of steady-state chlorophyll fluorescence for remote sensing detection of plant water, temperature and nitrogen stress, Remote Sensing of Environment, 168, 420–436, doi.org/10.1016/j.rse.2015.07.022, 2015.

Amante, C. and Eakins, B. W.: ETOPO1 arc-minute global relief model: procedures, data sources and analysis, 2009.

Berk, A., Bernstein, L. S., Anderson, G. P., Acharya, P. K., Robertson, D. C., Chetwynd, J. H., and Adler-Golden, S. M.: MODTRAN Cloud and Multiple Scattering Upgrades with Application to AVIRIS, Remote Sensing of Environment, 65, 367–375, doi.org/10.1016/S0034-4257(98)00045-5, 1998.

Berk, A., Acharya, P. K., Bernstein, L. S., Anderson, G. P., Jr, J. H. C., and Hoke, M. L.: Reformulation of the MODTRAN band model for higher spectral resolution, in: Algorithms for Multispectral, Hyperspectral, and Ultraspectral Imagery VI, Algorithms for Multispectral, Hyperspectral, and Ultraspectral Imagery VI, 190–198, doi.org/10.1117/12.410340, 2000.

Clark, R. N. and Swayze, G. A.: Automated Spectral Analysis: Mapping Minerals, Amorphous Materials, Environmental Materials, Vegetation, Water, Ice and Snow, and Other Materials: The USGS Tricorder Algorithm, 26, 255, 1995.

Coppo, P., Taiti, A., Pettinato, L., Francois, M., Taccola, M., and Drusch, M.: Fluorescence Imaging Spectrometer (FLORIS) for ESA FLEX Mission, Remote Sensing, 9, 649, doi.org/10.3390/rs9070649, 2017.

Damm, A., Erler, A., Hillen, W., Meroni, M., Schaepman, M. E., Verhoef, W., and Rascher, U.: Modeling the impact of spectral sensor configurations on the FLD retrieval accuracy of sun-induced chlorophyll fluorescence, Remote Sensing of Environment, 115, 1882–1892, doi.org/10.1016/j.rse.2011.03.011, 2011.

Daumard, F., Champagne, S., Fournier, A., Goulas, Y., Ounis, A., Hanocq, J.-F., and Moya, I.: A Field Platform for Continuous Measurement of Canopy Fluorescence, IEEE Transactions on Geoscience and Remote Sensing, 48, 3358–3368, doi.org/10.1109/TGRS.2010.2046420, 2010.

Dechant, B., Ryu, Y., Badgley, G., Köhler, P., Rascher, U., Migliavacca, M., Zhang, Y., Tagliabue, G., Guan, K., Rossini, M., Goulas, Y., Zeng, Y., Frankenberg, C., and Berry, J. A.: NIRVP: A robust structural proxy for sun-induced chlorophyll fluorescence and photosynthesis across scales, Remote Sensing of Environment, 268, 112763, doi.org/10.1016/j.rse.2021.112763, 2022.

Du, S., Liu, L., Liu, X., Zhang, X., Zhang, X., Bi, Y., and Zhang, L.: Retrieval of global terrestrial solar-induced chlorophyll fluorescence from TanSat satellite, Science Bulletin, 63, 1502–1512, doi.org/10.1016/j.scib.2018.10.003, 2018.

Du, S., Liu, L., Liu, X., Zhang, X., Gao, X., and Wang, W.: The Solar-Induced Chlorophyll Fluorescence Imaging Spectrometer (SIFIS) Onboard the First Terrestrial Ecosystem Carbon Inventory Satellite (TECIS-1): Specifications and Prospects, Sensors, 20, 815, doi.org/10.3390/s20030815, 2020.

Du, S., Liu, X., Chen, J., and Liu, L.: Prospects for Solar-Induced Chlorophyll Fluorescence Remote Sensing from the SIFIS Payload Onboard the TECIS-1 Satellite, Journal of Remote Sensing, 2022, doi.org/10.34133/2022/9845432, 2022.

Frankenberg, C., Butz, A., and Toon, G. C.: Disentangling chlorophyll fluorescence from atmospheric scattering effects in O2 A-band spectra of reflected sun-light, Geophys. Res. Lett., 38, L03801, doi.org/10.1029/2010GL045896, 2011a.

Frankenberg, C., Fisher, J. B., Worden, J., Badgley, G., Saatchi, S. S., Lee, J.-E., Toon, G. C., Butz, A., Jung, M., Kuze, A., and Yokota, T.: New global observations of the terrestrial carbon cycle from GOSAT: Patterns of plant fluorescence with gross primary productivity, Geophysical Research Letters, 38, doi.org/10.1029/2011GL048738, 2011b.

Frankenberg, C., O'Dell, C., Berry, J., Guanter, L., Joiner, J., Köhler, P., Pollock, R., and Taylor, T. E.: Prospects for chlorophyll fluorescence remote sensing from the Orbiting Carbon Observatory-2, Remote Sensing of Environment, 147, 1–12, doi.org/10.1016/j.rse.2014.02.007, 2014a.

Frankenberg, C., O'Dell, C., Berry, J., Guanter, L., Joiner, J., Köhler, P., Pollock, R., and Taylor, T. E.: Prospects for chlorophyll fluorescence remote sensing from the Orbiting Carbon Observatory-2, Remote Sensing of Environment, 147, 1–12, doi.org/10.1016/j.rse.2014.02.007, 2014b.

Guanter, L., Alonso, L., Gómez-Chova, L., Meroni, M., Preusker,R., Fischer, J., and Moreno, J.: Developments for vegetation fluorescence retrieval from spaceborne high-resolution spectrometry in the O2-A and O2-B absorption bands, J. Geophys. Res. Atmos., 115, D19303, doi:10.1029/2009JD013716, 2010.

Guanter, L., Frankenberg, C., Dudhia, A., Lewis, P. E., Gómez-Dans, J., Kuze, A., Suto, H., and Grainger, R. G.: Retrieval and global assessment of terrestrial chlorophyll fluorescence from GOSAT space measurements, Remote Sensing of Environment, 121, 236–251, doi.org/10.1016/j.rse.2012.02.006, 2012.

Guanter, L., Rossini, M., Colombo, R., Meroni, M., Frankenberg, C., Lee, J.-E., and Joiner, J.: Using field spectroscopy to assess the potential of statistical approaches for the retrieval of sun-induced chlorophyll fluorescence from ground and space, Remote Sensing of Environment, 133, 52–61, doi.org/10.1016/j.rse.2013.01.017, 2013.

Guanter, L., Zhang, Y., Jung, M., Joiner, J., Voigt, M., Berry, J. A., Frankenberg, C., Huete, A. R., Zarco-Tejada, P., Lee, J.-E., Moran, M. S., Ponce-Campos, G., Beer, C., Camps-Valls, G., Buchmann, N., Gianelle, D., Klumpp, K., Cescatti, A., Baker, J. M., and Griffis, T. J.: Global and time-resolved monitoring of crop photosynthesis with chlorophyll fluorescence, Proc Natl Acad Sci U S A, 111, E1327-1333, doi.org/10.1073/pnas.1320008111, 2014.

Guanter, L., Aben, I., Tol, P., Krijger, J. M., Hollstein, A., Köhler, P., Damm, A., Joiner, J., Frankenberg, C., and Landgraf, J.: Potential of the TROPOspheric Monitoring Instrument (TROPOMI) onboard the Sentinel-5 Precursor for the monitoring of terrestrial chlorophyll fluorescence, Atmospheric Measurement Techniques, 8, 1337–1352, doi.org/10.5194/amt-8-1337-2015, 2015.

Guanter, L., Bacour, C., Schneider, A., Aben, I., van Kempen, T. A., Maignan, F., Retscher, C., Köhler, P., Frankenberg, C., Joiner, J., and Zhang, Y.: The TROPOSIF global sun-induced fluorescence dataset from the Sentinel-5P TROPOMI mission, Earth System Science Data, 13, 5423–5440, doi.org/10.5194/essd-13-5423-2021, 2021.

Huete, A., Didan, K., Miura, T., Rodriguez, E. P., Gao, X., and Ferreira, L. G.: Overview of the radiometric and biophysical performance of the MODIS vegetation indices, Remote Sensing of Environment, 83, 195–213, doi.org/10.1016/S0034-4257(02)00096-2, 2002.

Hersbach, H., Bell, B., Berrisford, P., Hirahara, S., Horányi, A., Muñoz-Sabater, J., Nicolas, J., Peubey, C., Radu, R., Schepers, D., Simmons, A., Soci, C., Abdalla, S., Abellan, X., Balsamo, G., Bechtold, P., Biavati, G., Bidlot, J., Bonavita, M., De Chiara, G., Dahlgren, P., Dee, D., Diamantakis, M., Dragani, R., Flemming, J., Forbes, R., Fuentes, M., Geer, A., Haimberger, L., Healy, S., Hogan, R. J., Hólm, E., Janisková, M., Keeley, S., Laloyaux, P., Lopez, P., Lupu, C., Radnoti, G., de Rosnay, P., Rozum, I., Vamborg, F., Villaume, S., and Thépaut, J.-N.: The ERA5 global reanalysis, Quarterly Journal of the Royal Meteorological Society, 146, 1999–2049, doi.org/10.1002/qj.3803, 2020.

Inness, A., Ades, M., Agustí-Panareda, A., Barré, J., Benedictow, A., Blechschmidt, A.-M., Dominguez, J. J., Engelen, R., Eskes, H., Flemming, J., Huijnen, V., Jones, L., Kipling, Z., Massart, S., Parrington, M., Peuch, V.-H., Razinger, M., Remy, S., Schulz, M., and Suttie, M.: The CAMS reanalysis of atmospheric composition, Atmospheric Chemistry and Physics, 19, 3515–3556, doi.org/10.5194/acp-19-3515-2019, 2019.

Joiner, J., Yoshida, Y., Vasilkov, A. P., Yoshida, Y., Corp, L. A., and Middleton, E. M.: First observations of global and seasonal terrestrial chlorophyll fluorescence from space, Biogeosciences, 8, 637–651, doi.org/10.5194/bg-8-637-2011, 2011.

Joiner, J., Yoshida, Y., Vasilkov, A. P., Middleton, E. M., Campbell, P. K. E., Kuze, A., and Corp, L. A.: Filling-in of Far-Red and Near-Infrared Solar Lines by Terrestrial and Atmospheric Effects: Simulations and Space-Based Observations from

SCHIAMACHY and GOSAT, IEEE International Geoscience and Remote Sensing Symposium, Munich, NTRS Author Affiliations: NASA Goddard Space Flight Center, Science Systems and Applications, Inc., Maryland Univ. Baltimore County, Japan Aerospace Exploration Agency, Sigma Space Partners, LLCNTRS Report/Patent Number: GSFC.ABS.6134.2012NTRS Document ID: 20120009059NTRS Research Center: Goddard Space Flight Center (GSFC), 2012.

Joiner, J., Guanter, L., Lindstrot, R., Voigt, M., Vasilkov, A. P., Middleton, E. M., Huemmrich, K. F., Yoshida, Y., and Frankenberg, C.: Global monitoring of terrestrial chlorophyll fluorescence from moderate-spectral-resolution near-infrared satellite measurements: methodology, simulations, and application to GOME-2, Atmospheric Measurement Techniques, 6, 2803–2823, doi.org/10.5194/amt-6-2803-2013, 2013.

Joiner, J., Yoshida, Y., Guanter, L., and Middleton, E. M.: New methods for the retrieval of chlorophyll red fluorescence from hyperspectral satellite instruments: simulations and application to GOME-2 and SCIAMACHY, Atmospheric Measurement Techniques, 9, 3939–3967, doi.org/10.5194/amt-9-3939-2016, 2016.

Köhler, P., Guanter, L., and Joiner, J.: A linear method for the retrieval of sun-induced chlorophyll fluorescence from GOME-2 and SCIAMACHY data, Atmospheric Measurement Techniques, 8, 2589–2608, doi.org/10.5194/amt-8-2589-2015, 2015a.

Köhler, P., Guanter, L., and Frankenberg, C.: Simplified physically based retrieval of sun-induced chlorophyll fluorescence from GOSAT data, IEEE Geoscience and Remote Sensing Letters, 12, 1446–1450, doi.org/10.1109/LGRS.2015.2407051, 2015b.

Köhler, P., Frankenberg, C., Magney, T. S., Guanter, L., Joiner, J., and Landgraf, J.: Global Retrievals of Solar-Induced Chlorophyll Fluorescence With TROPOMI: First Results and Intersensor Comparison to OCO-2, doi.org/10.1029/2018GL079031, 2018.

Liu, L., Liu, X., Hu, J., and Guan, L.: Assessing the wavelength-dependent ability of solar-induced chlorophyll fluorescence to estimate the GPP of winter wheat at the canopy level, International Journal of Remote Sensing, 38, 4396–4417, doi.org/10.1080/01431161.2017.1320449, 2017.

Liu, X. and Liu, L.: Assessing Band Sensitivity to Atmospheric Radiation Transfer for Space-Based Retrieval of Solar-Induced Chlorophyll Fluorescence, Remote Sensing, 6, 10656–10675, doi.org/10.3390/rs61110656, 2014.

Li, X. and Xiao, J.: A Global, 0.05-Degree Product of Solar-Induced Chlorophyll Fluorescence Derived from OCO-2, MODIS, and Reanalysis Data, Remote Sensing, 11, 517, doi.org/10.3390/rs11050517, 2019.

Mohammed, G. H., Colombo, R., Middleton, E. M., Rascher, U., van der Tol, C., Nedbal, L., Goulas, Y., Pérez-Priego, O., Damm, A., Meroni, M., Joiner, J., Cogliati, S., Verhoef, W., Malenovský, Z., Gastellu-Etchegorry, J.-P., Miller, J. R., Guanter, L., Moreno, J., Moya, I., Berry, J. A., Frankenberg, C., and Zarco-Tejada, P. J.: Remote sensing of solar-induced chlorophyll fluorescence (SIF) in vegetation: 50 years of progress, Remote Sensing of Environment, 231, 111177, doi.org/10.1016/j.rse.2019.04.030, 2019.

Riggs, G., Hall, D., and Salomonson, V.: MODIS Snow products user guide to collection 5, Digital Media, 6, 2006.

Salomonson, V. V. and Appel, I.: Estimating fractional snow cover from MODIS using the normalized difference snow index, Remote Sensing of Environment, 89, 351–360, doi.org/10.1016/j.rse.2003.10.016, 2004.

Sun, Y., Frankenberg, C., Wood, J. D., Schimel, D. S., Jung, M., Guanter, L., Drewry, D. T., Verma, M., Porcar-Castell, A., Griffis, T. J., Gu, L., Magney, T. S., Köhler, P., Evans, B., and Yuen, K.: OCO-2 advances photosynthesis observation from space via solar-induced chlorophyll fluorescence, Science, 358, eaam5747, doi.org/10.1126/science.aam5747, 2017.

Taylor, T. E., Eldering, A., Merrelli, A., Kiel, M., Somkuti, P., Cheng, C., Rosenberg, R., Fisher, B., Crisp, D., Basilio, R., Bennett, M., Cervantes, D., Chang, A., Dang, L., Frankenberg, C., Haemmerle, V. R., Keller, G. R., Kurosu, T., Laughner, J. L., Lee, R., Marchetti, Y., Nelson, R. R., O'Dell, C. W., Osterman, G., Pavlick, R., Roehl, C., Schneider, R., Spiers, G., To, C., Wells, C., Wennberg, P. O., Yelamanchili, A., and Yu, S.: OCO-3 early mission operations and initial (vEarly) XCO2 and SIF retrievals, Remote Sensing of Environment, 251, 112032, doi.org/10.1016/j.rse.2020.112032, 2020.

van der Tol, C., Verhoef, W., Timmermans, J., Verhoef, A., and Su, Z.: An integrated model of soil-canopy spectral radiances, photosynthesis, fluorescence, temperature and energy balance, Biogeosciences, 6, 3109–3129, doi.org/10.5194/bg-6-3109-2009, 2009.

Vasilkov, A., Joiner, J., and Spurr, R.: Note on rotational-Raman scattering in the O_2A- and B-bands, Atmos. Meas. Tech., 6, 981–990, https://doi.org/10.5194/amt-6-981-2013, 2013.

Verhoef, W. and Bach, H.: Simulation of Sentinel-3 images by four-stream surface–atmosphere radiative transfer modeling in the optical and thermal domains, Remote Sensing of Environment, 120, 197–207, doi.org/10.1016/j.rse.2011.10.034, 2012.

Verhoef, W., van der Tol, C., and Middleton, E. M.: Hyperspectral radiative transfer modeling to explore the combined retrieval of biophysical parameters and canopy fluorescence from FLEX – Sentinel-3 tandem mission multi-sensor data, Remote Sensing of Environment, 204, 942–963, doi.org/10.1016/j.rse.2017.08.006, 2018.

Verrelst, J., Camps-Valls, G., Muñoz-Marí, J., Rivera, J. P., Veroustraete, F., Clevers, J. G. P. W., and Moreno, J.: Optical remote sensing and the retrieval of terrestrial vegetation bio-geophysical properties – A review, ISPRS Journal of Photogrammetry and Remote Sensing, 108, 273–290, doi.org/10.1016/j.isprsjprs.2015.05.005, 2015.

Vicent, J., Sabater, N., Tenjo, C., Acarreta, J. R., Manzano, M., Rivera, J. P., Jurado, P., Franco, R., Alonso, L., Verrelst, J., and Moreno, J.: FLEX End-to-End Mission Performance Simulator, IEEE Transactions on Geoscience and Remote Sensing, 54, 4215–4223, doi.org/10.1109/TGRS.2016.2538300, 2016.

Xu, S., Liu, Z., Zhao, L., Zhao, H., and Ren, S.: Diurnal Response of Sun-Induced Fluorescence and PRI to Water Stress in Maize Using a Near-Surface Remote Sensing Platform, Remote Sensing, 10, 1510, doi.org/10.3390/rs10101510, 2018.

Zhao, F., Ma, W., Köhler, P., Ma, X., Sun, H., Verhoef, W., Zhao, J., Huang, Y., Li, Z., and Ratul, A. K.: Retrieval of Red Solar-Induced Chlorophyll Fluorescence With TROPOMI on the Sentinel-5 Precursor Mission, IEEE Transactions on Geoscience and Remote Sensing, 60, 1–14, doi.org/10.1109/TGRS.2022.3162726, 2022a.

Zhao, F., Ma, W., Köhler, P., Ma, X., Sun, H., Verhoef, W., Zhao, J., Huang, Y., Li, Z., and Ratul, A. K.: Retrieval of Red Solar-Induced Chlorophyll Fluorescence With TROPOMI on the Sentinel-5 Precursor Mission, IEEE Transactions on Geoscience and Remote Sensing, 60, 1–14, doi.org/10.1109/TGRS.2022.3162726, 2022b.

Zheng, X., Zhao, W., Zhu, Z., Wang, Z., Zheng, Y., and Li, D.: Characterization and Evaluation of Global Solar-Induced Chlorophyll Fluorescence Products: Estimation of Gross Primary Productivity and Phenology, Journal of Remote Sensing, 4, 0173, doi.org/10.34133/remotesensing.0173, 2024.

Zou, C., Du, S., Liu, X., Liu, L., Wang, Y., and Li, Z.: Optimizing the Empirical Parameters of the Data-Driven Algorithm for SIF Retrieval for SIFIS Onboard TECIS-1 Satellite, Sensors, 21, 3482, doi.org/10.3390/s21103482, 2021.

Zou, C., Liu, L., Du, S., and Liu, X.: Investigating the Potential Accuracy of Spaceborne Solar-Induced Chlorophyll Fluorescence Retrieval for 12 Capable Satellites Based on Simulation Data, IEEE Transactions on Geoscience and Remote Sensing, 60, 1–13, doi.org/10.1109/TGRS.2022.3210185, 2022.